Title: Clinical and nano-analytical imaging identify calcified nodules as progression markers for age-related macular degeneration

Authors: Anna C.S. Tan, [#1,2,3,4] Matthew G. Pilgrim, [#5] Sarah Fearn,[6] Sergio Bertazzo,[7] Elena Tsolaki,[7] Alexander P. Morrell,[8] Miaoling Li,[9] Jeffrey D. Messinger,[9] Rosa Dolz-Marco,[1,2] Jianqin Lei,[10] Muneeswar G. Nittala,[10] Srinivas R. Sadda, [10, 11] Imre Lengyel, [†*5,12] K. Bailey Freund, [*1,2,13] and Christine A. Curcio [*9]

Affiliations:

1. Vitreous, Retina Macula, Consultants of New York, New York, NY, USA
2. LuEsther T Mertz Retinal Research Center, Manhattan, Eye, Ear and Throat Hospital, New York, NY, USA
3. Singapore National Eye Center/ Singapore Eye Research Institute Singapore, Singapore, Singapore
4. Duke-NUS Singapore, Singapore
5. UCL Institute of Ophthalmology, 11-43 Bath Street, London, EC1V 9EL, UK
6. Department of Materials, Imperial College London, London, SW7 2AZ, UK
7. Department of Medical Physics & Biomedical Engineering, University College London, Malet Place, Engineering Building, London WC1E 6BT, UK
8. Material Physics, Aston University, Aston Express Way, Birmingham, B4 7ET
9. Department of Ophthalmology, School of Medicine, University of Alabama at Birmingham, Birmingham, AL, USA
10. Doheny Image Reading Center, Doheny Eye Institute, Los Angeles, California, USA
11. Department of Ophthalmology, David Geffen School of Medicine at UCLA, Los Angeles, California, USA.
12. Centre for Experimental Medicine, School of Medicine, Dentistry and Biomedical Science, Queen's University Belfast, Belfast, BT9 7BL UK
13. Department of Ophthalmology, New York University Langone School of Medicine, New York, NY

# These authors contributed equally to this work; * co-senior; †corresponding author

Correspondence: Imre Lengyel, PhD; Centre for Experimental Medicine; School of Medicine, Dentistry and Biomedical Science; Queen's University Belfast, Belfast, BT9 7BL UK Queen's University Belfast; Tel: +44 (0) 28 9097 6027; (E): i.lengyel@ucl.ac.uk

Key Words: drusen, optical coherence tomography, autofluorescence, multimodal imaging, hydroxyapatite, calcium, phosphate, x-ray diffraction, histology, age-related macular degeneration

One Sentence Summary: Hydroxyapatite containing large nodules in the sub-RPE-basal laminar space are progression markers to end-stage age-related macular degeneration.

ABSTRACT

Soft drusen are a defining feature of age-related macular degeneration (AMD), a prevalent sight-threatening disease of older adults. In some eyes with AMD, optical coherence tomography shows heterogeneous internal reflectivity within soft drusen (HIRD). HIRD is associated with hypoautofluorescence of overlying retinal pigment epithelium (RPE) and a 4-fold increased risk of incident geographic atrophy at 1 year. We hypothesized that histologically imaged phosphate-rich multilobular refractile nodules (20-100 µm) might account for HIRD. Nano-analytical material science imaging techniques confirmed that calcium and phosphate form hydroxyapatite in nodules, as well as in spherules and Bruch's membrane plaques. However, nodules uniquely lack magnesium and represent polycrystalline hydroxyapatite, whereas spherules diffract as single crystal whitlockite, and plaques are amorphously crystalline. Nodules are high-risk biomarkers for rapid AMD progression and has a great potential to be used in clinical trials. The agonal state of the RPE overlying nodules impacts on the extracellular mineralization and this could be critical for developing new therapeutic approaches.

Introduction:

Globally, age-related macular degeneration (AMD) is a prevalent cause of legal blindness in the elderly. The neovascular form of advanced AMD is treatable, however, no effective treatment for the other form of advanced AMD, geographic atrophy (GA), is known. Clear ocular optics and sophisticated cellular-level clinical imaging techniques allow detailed study of disease microarchitecture in vivo. Biomarkers are indispensable for designing efficient clinical trials and for highlighting biological processes that may be targets to both prevent progression and treat advanced forms of AMD. Imaging methodologies based on high-speed optical coherence tomography (OCT) are being used to define biomarkers that may predict an increased risk of progression in eyes with intermediate AMD. These include extracellular drusen, subretinal drusenoid deposits, and intraretinal hyperreflective foci that represent migrating retinal pigment epithelium (RPE)[1]. Another previously identified biomarker, [1,2] heterogeneous internal reflectivity within drusen (HIRD), does not yet have a histologic and molecular correlate.

Drusen, which occur early in AMD, are lipid-, [3-7]mineral-[8,9] and protein-[10-13] containing extracellular deposits that accumulate between the basal lamina of the RPE and Bruch's membrane (BrM), i.e., in the sub-RPE-BL space. RPE cells support overlying photoreceptors and underlying choroidal vasculature, of which BrM, a layered extracellular matrix, is the innermost component. Three OCT reflectivity signatures in the sub-RPE-BL space and in BrM appear in eyes with GA: 1) small hyperreflective dots within drusen, [14] 2) HIRD, [2,15] and 3) hyperreflective lines near BrM. [16,17] Of these, HIRD are associated with increased risk for progression to advanced AMD (new atrophy at 6 months, odds ratio, 5.1; at last follow-up, odds ratio 7.0[2]). The precise tissue sources of these signals require definition.

Calcification (mineral deposition) capable of generating OCT reflectivity has been identified in AMD-affected tissues by various techniques, including light microscopy for refractility,

histochemical stains for phosphate and hydroxyapatite (HAP), and elemental and diffraction analysis for mineral components. Drusen contain 0.5-5.0 µm diameter spherules that are refractile, positive for von Kossa and HAP specific stains, [18,19] and produce a HAP-specific diffraction pattern when interrogated by synchrotron µ-X-ray diffraction. [8,9] BrM plaques contain calcium by elemental analysis,[19,20], but whether plaques generate reflectivity *in vivo* is unknown. One candidate OCT signature for plaques has been excluded in our ongoing clinicopathologic correlation studies, as highly hyperreflective lines near (and not in) BrM have been directly linked to cholesterol crystals. [21] A third structure comprises nodules, 20-100 µm in diameter, consisting of multiple lobes 1-20 µm in diameter, all refractile [14] and von-Kossa positive for phosphates.[22] Neither the mineral content nor an imaging signature is known for nodules. Based on spherules and BrM plaques, we expect that nodules also contain calcium phosphate.

Materials science techniques have successfully elucidated the composition and formation of early bone development, ectopic calcification in cardiovascular disease,[23,24] and HAP spherules in retinal drusen, which are almost certainly the hyperreflective dots seen in OCT.[14] We reasoned that this approach could also reveal composition and suggest formative processes of HIRD and plaques. Using a combination of clinical, histopathologic, and molecular imaging techniques, we determined that the HIRD progression biomarker is a nodule, i.e., a crystalline calcium phosphate mineral molecularly distinct from both spherules and plaques. A novel multi-modal imaging staging system for GA progression with associated evolving calcified drusen is proposed.

RESULTS

1: Multi-modal imaging appearance of potentially calcified structures

OCT signatures were contextualized through multimodal imaging. HIRD were identified on OCT within RPE elevations, occasionally associated with hyperreflective interior substructures (**Figure 1**: red arrow), non-refractile appearance on color fundus photography (CFP), isoautofluorescent in an area of confluent hypoautofluorescence on fundus autofluorescence (FAF) and non-reflective on near-infrared reflectance imaging (NIR). A thickened hyperreflective cap (pink arrowhead) that is non-refractile on CFP appears mildly hypoautofluorescent with a hyperautofluorescent ring on FAF, and is mildly hyperreflective on NIR. Hyperreflective dots within HIRD (green circle) are visible as glistening dots on CFP, which are occasionally hidden by the hyperreflective cap (pink arrow head). They are undetectable on FAF, and are hyperreflective on NIR. Hyperreflective lines that can be indistinguishable from BrM (blue arrowhead) are glistening on CFP, hypoautofluorescent on FAF, and highly reflective on NIR. Together HIRD and the overlying reflective caps were independently described in OCT as hyperreflective pyramidal structures [15] and C(onical)-type drusen [25]

Next, we report on four lines of investigation: 1) the association of HIRD with progression to advanced AMD; 2) *in vivo* and *ex vivo* OCT imaging-histology correlation of HIRD cores and caps; 3) composition of nodules, spherules, and BrM plaques based on high-resolution images, elemental analysis, and mineral phase identification; 4) natural history and confirmation of HIRD-associated RPE demise and AMD progression via multimodal longitudinal clinical imaging.

2: HIRD is associated with progression to advanced AMD

We began by determining the prognostic value of HIRD for advanced AMD. A total of 138 eyes of 131 patients (mean age 80.2 years ± 7.8; range, 63-96 years, 55 males and 76 females) with

intermediate AMD and sequential OCT data over 12 months from a tertiary care retinal practice in Los Angeles were analyzed for the presence of HIRD on dense volume OCT scans. Among these 138 eyes, 62 (45%) had evidence of at least one HIRD as seen on OCT. Fifty-five (40%) progressed to advanced AMD (defined as neovascular AMD or GA) within the next 12 months, including 33 which progressed to GA only, 14 which progressed to CNV only, and 8 which progressed to both atrophy and CNV. HIRD were significantly and independently associated with progression to advanced AMD at 12 months with an odds ratio of 4.22 (CI: 1.82 – 9.78; p = 0.001), highlighting the prognostic importance of HIRD for both end stages of advanced AMD.

3: Imaging-histology correlation of HIRD

We correlated OCT with histology in an eye recovered from a deceased donor 4 months after the last clinic visit (**Figure 2AB**, Case 1) and an eye from a clinically undocumented donor imaged with *ex vivo* OCT (**Figure 2EF**, Case 2**)**. In Case 1, HIRD corresponded to a multilobular nodule amidst typical soft druse contents, overlaid by RPE and thick basal laminar deposit (BLamD, thickened RPE basement membrane) (**Figure 2CD**). In Case 2, HIRD corresponded to a central nodule surrounded by proteinaceous material, covered by thin BLamD, absent RPE (**Figure 2G**) and atrophied photoreceptors **(Figure 2H**). To derive a plausible pathogenic sequence for HIRD, we examined images from an online resource for AMD histopathology (http://projectmacula) (**Figure 3**). We found that large nodules and isolated RPE cells appeared within the original lipidic contents of soft drusen, surrounded by a fibrous background (**Figure 3A, B**). Contents of individual drusen were replaced by nodules, (**Figure 3C-G)** as RPE coverage gradually decreased (**Figure 3C, D**), and BLamD persisted after RPE loss (**Figure 3E-G**). Drusen in **Figure 3C-G** have both nodules and spherules. Nodules tended to localize near the druse base but did not lie directly on BrM. However, within BrM, refractile plaques could be detected (**Figures 2G, 3A-G**). Thus, these studies established nodules as the basis of the HIRD signature.

4: The analysis of the composition of nodules, spherules, and BrM plaques

To investigate nodule composition a materials science approach was applied. This utilized scanning electron microscopy (SEM), energy dispersive x-ray spectroscopy (EDX), HAP specific fluorescent staining, secondary ion mass spectrometry (SIMS), synchrotron x-ray fluorescence and transmission electron microscopy-selected area electron diffraction (TEM-SAED).

One published AMD case [26] (**Supplementary Figure 1)** with a serous RPE detachment and RPE atrophy (**Supplementary Figure 1**) exhibited cloud-like pearly drusen and conventional soft drusen (**Supplementary Figure 1ABC**). A second published AMD case [27] possessed refractile nodules within micro-dissected macular soft drusen that were also amenable to analysis.

Nodules, spherules and plaques were first examined using SEM. Nodules **(Figure 4A, Supplementary Figure 2)** and spherules **(Figure 4B)** were readily visible on scanning electron micrographs due to their distinct morphology; however, plaques were not **(Figure 4CD).** Plaques were identifiable only by backscattered scanning electron microscopy, which showed dense material within BrM, likely mineralization **(Supplementary figure 3)**.

Lesions identified in these and other eyes were subsequently examined with EDX spectroscopy. Discrete peaks corresponding to P KL3, Ca KL3 and Ca KM2 were clearly identifiable on spectra obtained from spherules **(Figure 4L)**, plaques **(Figure 4M)**, and importantly for the first time, from nodules **(Figure 4K).** This suggests all 3 lesions are composed of an inorganic calcium phosphate. Peaks corresponding to carbon (C), oxygen (O), and sodium (Na) emanating from the mineralized lesions as well as from the surrounding organic soft tissues were also present **(Figure 4KLM).** A small discrete peak for magnesium (Mg) was also present on spectra from spherules and plaques; however, this peak was absent for nodules. To confirm

Ca and P as major components, we mapped the Ca KL3 and P KL3 peaks. Ca and P were enriched within nodules, spherules, and plaques, compared to the surrounding tissues **(Figure 4EH, Nodule; Figure 4FI, Spherule; Figure 4GJ, BrM plaque).**

Macular tissue with nodules, previously interrogated by *ex vivo* color imaging **(Supplementary Figure 1),** was also investigated with micro-focus synchrotron x-ray fluorescence to confirm the presence of Ca **(Supplementary Figure 4C)**.

Isolated nodules etched of resin and sectioned to 2 μm thickness were also characterized using time of flight-secondary ion mass spectrometry (TOF-SIMS). Typical ionic signatures including 39.9, 55.9, 102.9, 158.9, 174.9 and 230.8 m/z corresponding to $[Ca^+]$, $[CaO^+]$, $[CaPO_2^+]$, $[Ca_2PO_3^+]$, $[Ca_2PO_4^+]$, and $[Ca_3PO_5^+]$, respectively, were detected. It was previously reported that these signatures indicate inorganic HAP [28], suggesting nodules also contain this calcium phosphate compound. Molecular mapping of $[Ca^+]$, $[CaPO_2^+]$, and the sum of all detected CaP signatures confirmed the presence of calcium phosphate within nodules (**Supplementary figure 5)**.

Calcific lesions stained with apatite-specific OsteoSense 680EX (Perkin Elmer, USA) were imaged using confocal fluorescence microscopy. Nodules were heterogeneously stained, with crusts staining intensely (**Figure 4N,** arrowhead). As previously reported, [8,9] some spherules appeared to have a hollow core (**Figure 4O**). Plaques readily stained with Osteosense (**Figure 4P**). These results suggest that nodules, spherules and plaques were all composed of apatite.

The detection of secondary ions associated with HAP by TOF-SIMS as well as positive OsteoSense staining suggested HAP could be the major constituent of nodules. To explore the phases of calcium phosphate present in nodules, spherules and plaques, we employed transmission electron microscopy - selected area electron diffraction (SAED) on samples sectioned by a focused ion beam (FIB).

Each deposit was first characterized by TEM (**Figure 5A-I**). As observed by light microscopy, nodules had numerous lobes, ~1-20 µm in diameter (**Figure 5ADG**), each with a distinct electron-dense outer crust and a less electron-dense inner core (**Figure 5ADG**). Like nodules, spherules were also electron-dense with an inner core and a distinct outer shell (**Figure 5BE**). In contrast to lobular or round deposition in nodules and spherules, respectively, calcium phosphate deposition in BrM plaques appear as disordered and crosshatched crystal needles (**Figure 5CF**).

Subsequently, the calcium phosphate phases forming nodules, spherules and BrM plaques were determined using SAED (**Figure 5GHI**). Diffraction patterns obtained from nodules indicated a polycrystalline material composed of numerous unorganized crystals (**Figure 5G**). Diffraction rings including (002), (300), (211) and (006) confirmed that nodules were composed of HAP (**Supplementary table 2**). Spherules diffracted as a single crystal producing a spot pattern correlating to (010) zone axes of Whitlockite (**Figure 5H**). In contrast, BrM plaques produced diffuse rings indicating the presence of an amorphous material of very low crystallinity (**Figure 5I**). A diffuse ring encompassing multiple diffraction rings characteristic of apatite was detected (**Figure 5I**).

5: Multimodal imaging characterization and staging of HIRD

We then staged individual HIRD by longitudinal multimodal clinical imaging. We followed 97 HIRD in 21 eyes (per eye, mean 4.6, range 1-15) of 17 patients in a tertiary referral retinal clinic in New York City (6 men, 11 women, age at baseline 75.9 ± 10.4 years, range 58-94) for a mean of 6.17 years (range 3.2-7.5 years; mean number of consecutive OCT scans per eye, 22.9, range 10-62; total of 1198 B-scans). During this period, the number of lesions visible on CFP, NIR, and FAF all increased **(Supplementary Figure 6 & 7)**.

We proposed a novel 4-stage pathway for druse progression to HIRD **(Figure 6)**. Variation A has less, and Variation B has more, overlying BLamD, and similar trends were seen in both **(Supplementary Figures 6, 7; Supplementary Table 1)**.

Stage 1: druse under intact RPE and a thin layer of BLamD. Druse contents are homogenously and moderately hyperreflective, without evidence of a hyporeflective core. HAP spherules [9] are undetectable due to shadowing by the RPE, [14] the continuity of which is confirmed by FAF.

Stage 2A: a hyporeflective core representing a nodule under intact RPE and surrounded by hyperreflective dots. Within overlying retina, hyperreflective foci (migrating RPE) [29] are visible.

Stage 3A: focal loss of RPE, visible on OCT as disruption and thinning of the hyperreflective RPE-basal lamina band, gradually exposing the druse interior, which is reduced in volume. RPE loss is indicated by central hypoautofluorescence within a hyperautofluorescent border.

Stage 4A: complete loss of RPE overlying the nodule-filled druse, signified by absent FAF signal and a thin hyperreflective border of persistent BLamD.

Relative to variation A, variation B exhibited less refractility on CFP, more hyperautofluorescence, and less hyper-reflectivity on NIR **(Supplementary Figure 7)**. Most HIRD lesions were observed at Stages 2 and 3 **(Supplementary Figures 6,7)**.

DISCUSSION

Already a powerful tool to diagnose retinal disease, monitor progression, and provide end-points for clinical trials,[30] multimodal OCT-based clinical imaging can help define molecular pathogenesis if linked to the composition of visualized structures. Herein we replicate and extend a 2013 finding that HIRD associate with progression to advanced AMD, by applying the same imaging criteria to an independent cohort from the original practice. Further, we use histology, multi-modal clinical imaging, and high resolution molecular imaging to show that HIRDs are sprawling polycrystalline HAP nodules, distinctly different from the restricted sized spherules in drusen (**Supplementary Table 1**). **Figure 6** proposes that in the presence of high overall extracellular calcium concentration, higher extracellular magnesium concentration and an acidic pH might promote spherule formation while a lower magnesium concentration and neutral pH might promote nodule formation, as elaborated below. We further propose that the sub-RPE-BL space transforms to a nodule-promoting environment by release of Mg^{+2} as RPE cells die or migrate anteriorly atop drusen, [31] making HIRD indicators of RPE in its agonal state. This interpretation is supported by focal HIRD-associated hypoautofluorescence (**Figure 6**). Thus, progression risk is conferred not so much by HIRD themselves but by what they signify about RPE health.

Refractile drusen, appearing on ophthalmoscopy and CFP as glistening with reflective dots, were called "calcified" based on appearance and early studies using the von Kossa stain for phosphates. [26,32-34] These highly reflective features are associated with HIRD on OCT and higher rates of incidence of progression to advanced AMD in previous studies from our LA group, either alone or together with 3 other biomarkers.[1,2] OCT-reflective drusen substructures including type C(onical) resembling stage 4 HIRD (Figure 6) were associated with rapid progression to GA but not to neovascular AMD in a large cohort of patients with intermediate AMD, perhaps because only 14 individuals had this phenotype.[25] Our study expands this

11

literature by showing in the largest patient sample to date that the hyporeflective cores of drusen confer risk for advancement to both end-stages, and demonstrating that they are HAP nodules. By appearance and composition, nodules are not simply aggregations of recently described HAP spherules. [9] Unlike spherules, which are small, refractile on CFP, and reflective on OCT, nodules are large, refractile on CFP, and *non*-reflective on OCT, a difference possibly due to the nodules' rough surface and size. Nodules are hyporeflective like other calcified structures (50 μm – 1 mm) in the posterior eye. [35,36] We recommend that HIRD be called 'calcific nodules' going forward instead of an alternative term 'hyperreflective pyramidal structures.'[15] Our proposed term describes both the composition and structure of the hyporeflective core, which is now a proven biomarker of AMD progression. Further, HIRD can now be differentiated from lines with an Intense, mirror-like hyperreflectivity in or near BrM that also strongly associated with atrophy [16,17,37-39] and have been independently shown in our ongoing research to correlate to single or sparse cholesterol crystals. These crystals signify replacement of oily drusen with fluid or fibrotic contents that are sufficiently hydrated to support supersaturation and precipitation within the sub-RPE-basal laminar space. [21,40]

We observed distinct variations in calcium phosphate phases within specific deposits. Using x-ray diffraction, we previously reported HAP-enriched spherules in drusen [9] and in deposits formed by RPE cells in culture. [22] Combining TEM, EDX and SAED, we identified highly crystalline whitlockite spherules, polycrystalline HAP nodules, and poorly crystalline apatite plaques. Whitlockite, a magnesium-substituted calcium phosphate previously associated with several diseases [41-43] is herein reported for the first time in human eyes. Preferential whitlockite formation over HAP has been linked to acidic pH and increased magnesium (Mg) to calcium (Ca) ratio,[44,45] among other mechanisms. In the kidney, the frequency of apatite and whitlockite phases is unaffected by systemic Mg cation (Mg^{+2}) levels, [42] suggesting that local Mg^{+2} concentration determines which calcium phosphate phase forms. Therefore, appropriate

Mg^{+2} in the sub-RPE-BL space might promote formation of whitlockite spherules (**Figure 6**). Interestingly, Mg^{+2} can substitute a small proportion of Ca^{+2} in the HAP lattice causing inhibition of HAP crystal growth, [43,46] possibly explaining the restricted size of spherules. In contrast, the absence of Mg in nodules may signify that low local Mg^{+2} concentrations facilitate continued crystal growth and thus greater size. Finally, despite detectable Mg in plaques, the low crystallinity and association of plaque calcification with BrM collagen and elastin [19,47] did not allow calcium phosphate phases to be identified. Importantly, after examining numerous sub-RPE deposits of all sizes in our ongoing studies, we are yet to see one without spherules. Thus, we suggest that spherule formation is a natural endpoint for calcium phosphate formation, Mg^{+2} in the sub-RPE-BL space keeps crystal growth at bay, whereas reduced Mg^{+2} levels lead to continuous nodule growth (Figure 6). As depicted on Figure 3, spherules and nodules coexist, but nodules seem to be visible on OCT at the later stages of AMD progression compared to spherules. BrM plaques by their focal spatial confinement can be contrasted with widespread BrM calcification in the inherited disorder pseudoxanthoma elasticum (OMIM 264800), [48] suggesting again local pathogenic regulation of mineralization within the druse. In pseudoxanthoma elasticum, BrM is reflective with a rough surface on OCT; [49] whether the smaller plaques in AMD will be similarly visible is not yet known.

What extracellular factors potentially modulate apatite formation in AMD? Organic molecules like functional groups of amino acids, as part of proteins in solution,[50,51] can inhibit HAP formation. However, when immobilized or entrapped on surfaces,[51,52] like in aged BrM, proteins can promote mineral deposition. Similarly, lipids can also nucleate mineral deposition, including both HAP and whitlockite. [53-55] Lipids and lipoproteins are abundant in soft drusen [7,11,12]. Direct support for lipid-associated mineralization includes the identification of a cholesterol core within spherules [9] as well as detection of phosphatidylcholine within sub-RPE deposits produced by confluent and functional RPE cells in culture. [22] Whilst the mechanism(s) and full

range of contributory proteins and lipids are yet to be identified, our data support a model of organic molecules nucleating mineral deposits. Once seeded, mineralized surfaces could become sites for further protein deposition.[9,22] Independent of the seeding mechanisms, Ca and P supersaturation is essential to initiate mineralization. In tissues, Ca availability is tightly regulated with high affinity binding proteins [56] and extracellular phosphate concentration is low. [57,58] Nevertheless, we observed HAP deposition by RPE cells cultured under standard conditions, suggesting that seemingly healthy RPE cells establish an environment conducive to mineral nucleation and growth. [22] How HAP deposition occurs *in vitro* and whether whitlockite formation can be promoted by modulating culture medium pH and Mg concentration can now be investigated.

Under "normal" circumstances neither Mg nor Ca are available for mineralization. However, with aging, especially pathological aging, this appear to change. For mineralization to take place there needs to be high concentration of available Ca^{+2}. In the presence of sufficient extracellular Mg^{+2}, spherules are formed due to the presence of functional RPE overlying drusen. At low extracellular Mg^{+2} and high Ca^{+2}, a condition that might be associated with increasingly non-functional RPE overlying drusen, the Mg control of mineral growth is lost and nodules start proliferating. In addition to extracellular nucleation, we also consider intracellular mechanisms that might promote Ca^{+2}-Mg^{+2} imbalance and calcification in the sub-RPE-BL space, focusing attention on mitochondria. High calcium stores in mitochondria along with ultrastructurally visible microparticles of tricalcium phosphate suggested a role in extracellular HAP deposition in both health (e.g., bone) and in tissue injury. [59] This idea has received recent support with nano-analytic techniques applied to osteoblasts in culture. [60] Mitochondrial calcium stores released by failing RPE cells could exit to the extracellular sub-RPE-BL space and tip the Ca^{+2}-Mg^{+2} balance towards nodule formation in AMD. The number of human RPE mitochondria declines with age, [61] especially in the macula. This decline is related to AMD severity and

mitochondrial DNA is damaged. [62,63] Opening of the mitochondrial permeability transition pore leads to swelling, rupture, and release of mitochondrial contents, including Ca^{+2}, into the cytosol. [64] A decrease in the levels of DICER1 in AMD eyes results in accumulated Alu-RNA, which is in turn associated with cytosolic release of mitochondrial DNA and presumably Ca^{+2} also. [65,66] Interestingly, a review of data obtained from our RPE culture system failed to confirm the presence of Mg^{+2} within the *in vitro* mineralized deposits, suggesting that even these apparently functional cells are stressed and in Ca^{+2}-Mg^{+2} imbalance. [22]

Pathways regulating sub-RPE Ca and Mg concentrations are unknown, suggesting aspects of cellular physiology needing exploration. Ca signaling by the RPE is well-studied and essential to the activity of apical and basolateral potassium and chloride channels that collectively regulate the ionic environment of photoreceptors, photoreceptor-RPE adherence, and net fluid efflux from retina to choroid. [67] Ca signaling is also important for health of lysosomes [68] needed for RPE processing of ingested photoreceptor tips and diet-delivered lipids. Mg homeostasis is less well studied, although in its ionic form, Mg^{+2} is required by many kinases, including those involved in maintaining apically located, inward-rectifying potassium currents in RPE. [69,70] Further, developmental Mg deficiency causes focal RPE degeneration and excess Ca/Mg ratio in retina.[71]

We do not yet have an OCT correlate for BrM plaques in AMD, of interest because BrM calcification and rupture is thought to promote neovascularization. [72] Vascular calcification is well-established in atherosclerotic cardiovascular disease, and nano-analytical imaging studies suggest that microcalcification along collagen and elastin fibers in intima is critical to the evolution of coronary lesions at risk for rupture.[24,73,74] Atherosclerosis and AMD share commonalities of sub-endothelial lipoprotein deposition (in arterial intima and BrM), despite disassociation of top-level biologic risk factors (e.g., plasma LDL levels, apoE4 genotype), a paradox attributed to intraocular cholesterol and lipoprotein gene expression serving eye-

specific physiology.[75,76] Higher resolution OCT may someday allow visualization of BrM plaques and the understanding how these are associated with AMD.

In summary, e*x vivo* imaging showed 3 distinct refractile structures associated with GA: 1) small highly crystalline whitlockite spherules that account for hyperreflective dots on OCT and NIR, 2) large nodules containing polycrystalline calcium phosphate and appearing hyporeflective on OCT and iso-reflective on NIR, and 3) amorphous crystalline plaques in BrM without an OCT imaging signature in AMD. Common features amongst these are the Ca and P containing mineralization underpinned by previously unidentified molecular processes. Our proposed novel pathways for the mineralization in the sub-RPE-BL space are supported by multi-modal clinical and nano-analytic imaging and linked to histology (**Supplementary Table 1**). Current data on the role of calcium in AMD pathogenesis are fragmentary. Calcium consumption has been associated with both increased prevalence[77] and reduced incidence of late AMD, [78] and usage of calcium channel blockers was shown to increase AMD incidence. [79] While the role of calcification in AMD thus needs further investigation, mineralomic research in atherosclerotic cardiovascular disease may provide a framework for discovering the molecular mechanisms resulting in progression to late AMD. Clinical detection of calcification in multi-modal ophthalmic imaging may elucidate the relationship between local and systemic Ca^{+2} and Mg^{+2} regulation, oral supplementation, and the utility of targeting these processes for AMD treatment and prevention.

Materials and Methods

Clinical cohort of eyes with AMD

Both clinical cohorts were approved by their respective Institutional Review Boards and complied with the Health Insurance Portability and Accountability Act of 1996 and the Declaration of Helsinki.

Clinical cohort of eyes with intermediate AMD

To establish the prevalence of HIRD, a cohort of a total of 840 eyes of 420 consecutive patients with AMD seen by a single retinal specialist (SRS) between 2010 and 2014 in a tertiary care academic retinal practice in Los Angeles was retrospectively reviewed. From this dataset, we selected all subjects who had at least one eye with evidence of intermediate AMD (defined according to the Beckman classification)[80], no other posterior segment ocular disease, dense OCT volume scans (Cirrus OCT with 128 B-scans over a 6x6 mm region centered on the fovea), and at least 12 months of follow-up data including OCT. Dense volume scans with this spacing of just under 50 μm between scans was required in order avoid missing the center of large drusenoid lesions between the B-scans, which was critical for reliable assessment of druse core reflectivity characteristics. Twelve months of follow-up data was required. When both eyes of one subject met these inclusion criteria, one eye was randomly selected for analysis. A total of 138 eyes from 138 subjects met these criteria. OCT scans at baseline were reviewed by certified OCT graders at the Doheny Image Reading Center to assess for presence of hyporeflective cores within the drusen. Graders were masked as to other clinical data regarding the patients. Clinical charts and follow-up imaging data were evaluated over the next 12 months to ascertain the frequency of progression GA or CNV.

Study cohort for multimodal imaging of 100 defined deposits

To establish stages of deposit progression, a cohort of consecutive patients with heterogeneous internal reflectivity in drusen (HIRD) on OCT imaging, seen by a single retinal specialist (KBF) at a tertiary private retinal practice, was retrospectively reviewed.

Inclusion criteria were eyes with GA with at least one HIRD seen on OCT with at least a 3 year follow up with OCT volume scans taken on at least 10 consecutive visits. The exclusion criteria included presence of any neovascular AMD during the course of follow up, other retinal vascular or degenerative diseases, and eyes with significant media opacity that affected imaging quality.

Multimodal imaging protocol and analysis

Detailed assessment of medical records and multimodal imaging including color fundus photography (CFP), fundus autofluorescence (FAF), near-infrared reflectance (NIR) and OCT was performed on all the patients. CFP and FAF were performed with a TRC-50IX flood-illuminated fundus camera (Topcon Corp, Tokyo, Japan). In some cases, FAF and in all cases spectral domain OCT imaging with corresponding NIR images was performed on Spectralis HRA+OCT scanning laser ophthalmoscope with OCT (Heidelberg Engineering, Heidelberg, Germany). Serial eye-tracked OCT scans were used to perform retrospective qualitative analysis from the baseline visit until the most recent visit, where the HIRD were detected. The OCT scanning protocol used in all eyes comprised 20˚ horizontal raster line scans over the area of interest ranging from 19-73 B-scans per eye, each scan spaced 62 to 250 µm apart depending on scan density, with automatic real-time averaging set between 5 and 12.

To analyze HIRD, the most recent OCT B-scan that best represented the HIRD was identified and serial eye-tracked B-scans of that specific area was then extracted from the most recent visit back in time until the baseline visit. In cases where the scanning protocol varied during follow-up, the B-scan closest to the area of interest was matched manually and extracted for

analysis. Extracted OCT images and corresponding NIR images were then stacked, aligned and saved as a video file using FIJI ("Fiji is just Image J," http://fiji.sc) [81] for qualitative analysis of lesion progression (see **Supplementary Video**). During the various time points, HIRD appearance on OCT was correlated to the appearance on CFP, NIR and FAF.

The features on OCT seen such as the hyporeflective core, hyperreflective dots and hyperreflective needle like plaques were assessed for their location in the RPE-basal lamina-BrM complex. Deep structures were defined as those that were located directly adjacent but within the axial resolution of the spectral domain OCT and in contact with the BrM and superficial structures were defined as those located above the BrM. HIRD seen on CFP was graded as a binary variable of refractile (1) versus non-refractile (0). [14] HIRD seen on NIR imaging was graded as non-reflective (0), mildly hyperreflective (1) and highly hyperreflective (2) (this can include focal or confluent areas of hyper-reflectivity). HIRD seen on FAF was graded as hypoautofluorescent (0), isoautofluorescent (1) and hyperautofluorescent (2). In cases where lesions had a mixed appearance such as a border or hyperautofluorescence with a central area of hypoautofluorescence the appearance of the majority of the lesion determined the final grade.

Imaging-histology correlations in donor eyes with AMD

Spectral domain OCT imaging of human donor eyes followed by high-resolution histology provided a link between clinical imaging and microanalysis of selected drusen. Three separate series of eyes were reviewed for suitable specimens, all drawn from a repository of ≥900 pairs of donor eyes accessioned from the Alabama Eye Bank for research purposes 1995-2012. 1) Eyes for OCT imaging and histology **(Figures 2-3)** were used for the creation of the Project MACULA online AMD histology resource (http://projectmacula), 142 maculas (82 AMD, 60 age-matched controls), median death-to-preservation time was 3.62 hours (range, 0.67-12.15

hours). These were subject to *ex vivo* multimodal imaging including OCT, NIR, and 488 nm and 787 nm FAF, using a custom tissue holder and a Spectralis HRA+OCT (Heidelberg Engineering, Heidelberg Germany), in addition to digital color photography.[40] Specimens were post-fixed in osmium tannic acid paraphenylenediamine to preserve extracellular lipid, embedded in epoxy resin, sectioned at 0.8 µm, and stained with toluidine blue.[26] 2) For advanced mineralomics, one eye with distinctive glistening drusen from the ALARMGS series of eyes (n=30)[26] was used and shown in **Supplementary Figure 1**. All eyes underwent *ex vivo* color imaging using epi- and trans-scleral illumination, followed by post-fixation in osmium only, en bloc staining with uranyl acetate, and epoxy embedding. 3) Large macular drusen previously imaged by *ex vivo* color reflectance photography, micro-dissected, and histologically confirmed as having mineralized contents were used for advanced mineralomics in **Figures 4-5**.[27] In this series of 9 eyes of 7 donors, macular soft drusen were manually isolated and post-fixed by the osmium tannic acid paraphenylenediamine method.

In addition to these clinically undocumented eyes, the left eye of a patient with *in vivo* clinical OCT was used for direct clinicopathologic correlation **(Figure 2A-D).** An 86-year-old white woman had geographic atrophy in the left eye. Four months after the last clinic visit, and 7:30 hr after death, eyes were recovered and preserved by perfusion as described.[82] Histological preparation was the same as the first series described above.

Sample source for mineralomic studies

After acquiring ethical approval, human cadaveric eyes with sub-RPE deposits and Bruch's membrane plaques were obtained from the University College London Institute of Ophthalmology and Moorfield's Eye Hospital Tissue Repository. Cadaveric eyes were enucleated 12-24 hours after death and preserved in 1% glutaraldehyde with 4% paraformaldehyde. Spherules, nodules, and plaques were identified in these specimens by

comparison of morphology to specimens with clinical and/ or *ex vivo* imaging documentation of AMD with large macular drusen, as described above.

Scanning electron microscopy and Energy dispersive x-ray spectroscopy

Scanning electron microscopy was performed on fixed, paraffin-embedded human cadaveric tissues and on isolated nodules embedded in epoxy resin. Human cadaveric tissues were sectioned at a thickness of 10 μm and collected on glass slides. Paraffin wax was removed by washing with xylene, followed by dehydration in a graded alcohol series (30, 50, 70, 90, 100% Ethanol) and chemical critical point drying with hexamethyldisilazane (Sigma Aldrich, USA) for 5 minutes. Tissues were then air-dried in a fume hood for 1 hour at room temperature. Isolated nodules were fixed and dehydrated prior to embedding in epoxy resin. Embedded nodules were sectioned at a thickness of 2 μm using an ultramicrotome (Leica Biosystems, Germany) and collected on glass slides. Epoxy resin was then etched from the isolated nodules using sodium methoxide (Sigma Aldrich, USA).

After dehydration and etching, glass slides with tissues were mounted on aluminum stubs (Agar Scientific, UK) using double-sided carbon adhesive tabs (Agar Scientific, UK). To ensure conductivity of the sample, double-sided conductive copper tape was used to form a bridge between the underside of the stub and the glass surface (Agar Scientific, UK). Samples were then sputter coated with a 1 nm thick layer of platinum.

Scanning electron microscopy was performed on a Zeiss Sigma VP scanning electron microscope (Carl Zeiss AG, Germany) equipped with a secondary electron detector and a backscattered electron detector. High-resolution images were obtained using the secondary electron detector whilst density differences were imaged using the backscattered electron detector. For secondary electron imaging, an accelerating voltage of 3 kV, an aperture of 30 μm and a working distance of 2-4 mm were used. For backscattered electron imaging, an

accelerating voltage of 10-15 kV, an aperture of 120 mm, and a working distance of 8-10 mm were used.

Density dependent colored-scanning electron micrographs (DDC-SEM) were generated post-acquisition of electron micrographs. Micrographs were collected with a secondary electron detector and the identical region captured using a backscattered electron detector. The secondary electron micrographs provide high-resolution details of the tissue whilst the backscattered electron micrographs provide information regarding density changes within the sample. Regions of red/orange color observed on DDC images indicate areas of dense material, likely mineral, whilst green indicates soft tissues.

Energy dispersive x-ray spectroscopy was performed on a Philips XL30 FEG-SEM (FEI, USA) equipped with an energy dispersive x-ray spectroscopy elemental analysis system (Oxford Instruments, UK). An accelerating voltage of 20 kV and a spot size of 5 was used. Samples were coated with platinum or carbon over gold/palladium to avoid overlapping of the KL3 phosphorus energy emission with the low emission energies of gold.

Secondary ion mass spectrometry of calcific lesions

To ensure samples suitable for the ultra-high vacuum conditions required for secondary ion mass spectrometry, tissues were dehydrated as described for scanning electron microscopy. Time of flight – secondary ion mass spectrometry (TOF-SIMS) and secondary ion mapping was conducted using a TOF.SIMS5-Qtac100 LEIS mass spectrometer (ION-TOF, Munster, Germany). A bismuth primary ion beam with an incident energy of 25 kV and operating with a Bi3+ cluster ion source was employed for greater secondary ion yield. For charge compensation, a low energy electron flood gun was used. Secondary molecular ions 0-880 m/z were mapped at sub-micron resolution using software supplied by ION-TOF.

Synchrotron microfocus x-ray fluorescence

Synchrotron micro-focus x-ray fluorescence experiments were conducted on beamline [83] at Diamond light source, Didcot, UK. Epoxy resin-embedded cross-sections were mounted on silicon nitride membrane windows (membrane, 5.0 x 5.0 mm, 500 nm thick; Silson, UK) as these contained no detectable contaminating metals. Incident beam energy of 17.15 keV was used to excite the elements of interest, with a focused spot size of 2.5 μm x 2.5μm (H x V), and a photon flux of 5.8e+10 photons/second. The beam was raster scanned over the region of interest with an acquisition time of 1 second per point and a step size of 1 μm in both vertical and horizontal directions. The fluorescence signal from the sample was detected using a 4-element SI drift fluorescence detector. Raw data were recorded in NeXus format using Diamond Light Source software. Analysis and generation of elemental maps were performed using PyMca, a multiplatform software package developed by the ESRF, Grenoble [84].

Hydroxyapatite specific fluorescent labelling of calcific lesions

Isolated nodules and cadaveric tissues known to contain calcium phosphate lesions were stained with Osteosense 680EX (Perkin Elmer, USA), a fluorescent bisphosphonate imaging agent used to observe ectopic calcifications. Prior to staining, isolated nodules embedded in epoxy resin were sectioned at a thickness of 200 nm using a Leica RM2225 Ultramicrotome, collected on glass slides, and washed in distilled water. For fixed and paraffin embedded human cadaveric tissues, 10 μm thick cross sections were generated, dewaxed in xylene, and rehydrated with a graded alcohol series. Both sample types were then incubated with Osteosense 680EX diluted in distilled water (Dilution: 0.002 nm/μl) for 20 minutes, at room temperature and in the dark. After incubation with OsteoSense, samples were washed with distilled water for 10 minutes, and mounted in 70% glycerol diluted in PBS. Stained samples

were imaged using a Leica TCS SP8 confocal laser-scanning microscope and a 63X oil immersion lens. An excitation wavelength of 668 nm and an emission wavelength of 687 nm were used.

Focused ion beam milling of cadaveric tissues

To generate 100 nm cross sections suitable for TEM-SAED, samples containing calcific lesions of interest were milled using a focused ion beam (FIB). Use of a focused ion beam prevents artefactual damage to the atomic arrangement of the mineral deposits of interest and thus prevents false results. Carbon sputtered samples were used, as platinum or gold sputtering prevents ion beam milling. FIB milling was performed on FEI Helios NanoLab DualBeam (FEI Corporate, Oregon, USA).

In advance of FIB milling, 15 x 2 μm regions containing calcific lesions of interest (nodule, spherules or BrM plaques) were coated with a 2 μm thick layer of platinum. Application of a platinum coat ensured lesions were protected whilst milling was completed. FIB milling was performed using a gallium ion (Ga+) source at a current of 2.8 nA and a resolution of ~5-10 nm. Tissue adjacent to the platinum protected tissue was milled to a depth of 10 μm and a width of 2 μm along the entire length of the platinum coat. Upon generating a 15 μm thick section beneath the platinum coat, the sample was rotated 90 degrees and the sample thinned to 100 nm. Thinning of the section was achieved using the Ga+ beam at a current of 28 pA to 2.8 nA. After thinning, sections were collected on to copper grids using the OmniProbe Autoprobe 200 in-situ lift-out system (Oxford Instruments, UK). Milled sections were collected on OmniProbe lift-out copper grids (Oxford Instrument, UK) designed to fit standard TEM grid holders. Platinum coating was used to fix the OmniProbe to the sample. The Ga+ beam was then used to detach the section attached to the OmniProbe from the sample. Platinum was then applied to the

OmniProbe lift-out copper grid and the sample attached. The Ga+ beam was then used to detach the OmniProbe was the section and copper grid.

Transmission electron microscopy – selected area electron diffraction

The mineral phase of isolated nodules, spherules and Bruch's membrane plaques were determined using selected area electron diffraction (SAED). SAED was performed on a JEOL 2000FX TEM operating with an acceleration voltage of 120 kv.

Supplementary Material:

Figure S1: Refractile drusen with nodules and RPE atrophy in the index case for microanalysis.

Figure S2. Scanning electron microscopy of isolated nodules.

Figure S3. Density dependent color – scanning electron microscopy of calcific lesions.

Figure S4. Synchrotron microfocus x-ray fluorescence confirms the presence of Ca in large nodules.

Figure S5. Time of flight-secondary ion mass spectrometry confirms the presence of calcium phosphate within nodules**.**

Figure S6: Appearance of heterogeneous internal reflectivity in drusen (HIRD) as seen on multimodal imaging during progression.

Figure S7: Appearance of heterogeneous internal reflectivity in drusen (HIRD)

Table S1: Composition and appearance of calcified structures in eyes with geographic atrophy as revealed by multi-modal clinical and molecular imaging.

Table S2: D spacings and I/Imax (%, 3 d.p.) of candidate calcium phosphate compounds.

MOVIE S1: Serial eye-tracked optical coherence tomography scans.

REFERENCES

1. Lei J, Balasubramanian S, Abdelfattah NS, Nittala M, Sadda SR. Proposal of a simple optical coherence tomography-based scoring system for progression of age related macular degeneration. *Graefes Arch Clin Exp Ophthalmol.* 2017;255(8):1551-1558.

2. Ouyang Y, Heussen FM, Hariri A, Keane PA, Sadda SR. Optical coherence tomography-based observation of the natural history of drusenoid lesion in eyes with dry age-related macular degeneration. *Ophthalmology.* 2013;120(12):2656-2665.

3. Farkas TG, Sylvester V, Archer D, Altona M. The histochemistry of drusen. *American Journal of Ophthalmology.* 1971;71(6):1206-1215.

4. Pauleikhoff D, Zuels S, Sheraidah GS, Marshall J, Wessing A, Bird AC. Correlation between biochemical composition and fluorescein binding of deposits in Bruch's membrane. *Ophthalmol.* 1992;99(10):1548-1553.

5. Curcio CA, Millican CL, Bailey T, Kruth HS. Accumulation of cholesterol with age in human Bruch's membrane. *Invest Ophthalmol Vis Sci.* 2001;42(1):265-274.

6. Haimovici R, Gantz DL, Rumelt S, Freddo TF, Small DM. The lipid composition of drusen, Bruch's membrane, and sclera by hot stage polarizing microscopy. *Invest Ophthalmol Vis Sci.* 2001;42(7):1592-1599.

7. Curcio CA, Presley JB, Malek G, Medeiros NE, Avery DV, Kruth HS. Esterified and unesterified cholesterol in drusen and basal deposits of eyes with age-related maculopathy. *Exp Eye Res.* 2005;81(6):731-741.

8. Flinn JM, Kakalec P, Tappero R, Jones B, Lengyel I. Correlations in distribution and concentration of calcium, copper and iron with zinc in isolated extracellular deposits associated with age-related macular degeneration. *Metallomics.* 2014;6(7):1223 - 1228.

9. Thompson RB, Reffatto V, Bundy JG, et al. Identification of hydroxyapatite spherules provides new insight into subretinal pigment epithelial deposit formation in the aging eye. *Proc Natl Acad Sci U S A.* 2015;112(5):1565-1570.

10. Crabb JW, Miyagi M, Gu X, et al. Drusen proteome analysis: an approach to the etiology of age-related macular degeneration. *Proc Natl Acad Sci U S A.* 2002;99(23):14682-14687.

11. Malek G, Li C-M, Guidry C, Medeiros NE, Curcio CA. Apolipoprotein B in cholesterol-containing drusen and basal deposits in eyes with age-related maculopathy. *Am J Pathol.* 2003;162(2):413-425.

12. Wang L, Clark ME, Crossman DK, et al. Abundant lipid and protein components of drusen. *PLoS ONE.* 2010;5(4):e10329.

13. Fett AL, Hermann MM, Muether PS, Kirchhof B, Fauser S. Immunohistochemical localization of complement regulatory proteins in the human retina. *Histology and histopathology.* 2012;27(3):357-364.

14. Suzuki M, Curcio CA, Mullins RF, Spaide RF. Refractile drusen: clinical imaging and candidate histology. *Retina.* 2015;35(5):859-865.

15. Bonnet C, Querques G, Zerbib J, et al. Hyperreflective pyramidal structures on optical coherence tomography in geographic atrophy areas. *Retina.* 2014;34(8):1524-1530.

16. Fleckenstein M, Charbel Issa P, Helb HM, et al. High-resolution spectral domain-OCT imaging in geographic atrophy associated with age-related macular degeneration. *Invest Ophthalmol Vis Sci.* 2008;49(9):4137-4144.

17. Moussa K, Lee JY, Stinnett SS, Jaffe GJ. Spectral domain optical coherence tomography-determined morphologic predictors of age-related macular degeneration-associated geographic atrophy progression. *Retina.* 2013;33(8):1590-1599.

18.	Ulshafer RJ, Allen CB, Nicolaissen B, Jr., Rubin ML. Scanning electron microscopy of human drusen. *Invest Ophthalmol Vis Sci.* 1987;28(4):683-689.

19.	van der Schaft TL, de Bruijn WC, Mooy CM, Ketelaars DAM, de Jong PTVM. Element analysis of the early stages of age-related macular degeneration. *Archives of Ophthalmology.* 1992;110(3):389-394.

20.	Davis WL, Jones RG, Hagler HK. An electron microscopic histochemical and analytical X-ray microprobe study of calcification in Bruch's membrane from human eyes. *J Histochem Cytochem.* 1981;29(5):601-608.

21.	Li M, Dolz-Marco R, Huisingh C, et al. Clinicopathologic correlation of geographic atrophy secondary to age-related macular degeneration. *Ophthalmology.*6/1/18 submitted.

22.	Pilgrim MG, Lengyel I, Lanzirotti A, et al. Sub-retinal pigment epithelial deposition of drusen components including hydroxyapatite in a primary cell culture model. *Invest Ophthalmol Vis Sci.* 2017;58(2):708–719.

23.	Fratzl P, Weinkamer R. Nature's hierarchical materials. *Prog Material Sci.* 2007;52(8):1263-1334.

24.	Bertazzo S, Gentleman E, Cloyd KL, Chester AH, Yacoub MH, Stevens MM. Nano-analytical electron microscopy reveals fundamental insights into human cardiovascular tissue calcification. *Nat Mater.* 2013;12(6):576-583.

25.	Veerappan M, El-Hage-Sleiman AM, Tai V, et al. Optical coherence tomography reflective drusen substructures predict progression to geographic atrophy in age-related macular degeneration. *Ophthalmology.* 2016;123(12):2554-2570.

26.	Curcio CA, Medeiros NE, Millican CL. The Alabama Age-related Macular Degeneration Grading System for donor eyes. *Invest Ophthalmol Vis Sci.* 1998;39(7):1085-1096.

27.	Rudolf M, Clark ME, Chimento M, Li C-M, Medeiros NE, Curcio CA. Prevalence and morphology of druse types in the macula and periphery of eyes with age-related maculopathy. *Invest Ophthalmol Vis Sci.* 2008;49(3):1200-1209.

28.	Malmberg P, Nygren H. Methods for the analysis of the composition of bone tissue, with a focus on imaging mass spectrometry (TOF-SIMS). *Proteomics.* 2008;8(18):3755-3762.

29.	Balaratnasingam C, Messinger JD, Sloan KR, Yannuzzi LA, Freund KB, Curcio CA. Histologic and optical coherence tomographic correlations in drusenoid pigment epithelium detachment in age-related macular degeneration. *Ophthalmology.* 2017;124(1):644- 656.

30.	Rosenfeld PJ. Optical coherence tomography and the development of antiangiogenic therapies in neovascular age-related macular degeneration. *Invest Ophthalmol Vis Sci.* 2016;57(9):OCT14-26.

31.	Curcio CA, Zanzottera EC, Ach T, Balaratnasingam C, Freund KB. Activated retinal pigment epithelium, an optical coherence tomography biomarker for progression in age-related macular degeneration. *Invest Ophthalmol Vis Sci.* 2017;58(6):BIO211-BIO226.

32.	Gass JDM. Pathogenesis of disciform detachment of the neuroepithelium. III. Senile disciform macular degeneration. *Am J Ophthalmol.* 1967;63:617-644.

33.	Green WR, Key SN, 3rd. Senile macular degeneration: a histopathologic study. *Trans Am Ophthalmol Soc.* 1977;75:180-254.

34.	Bressler NM, Silva JC, Bressler SB, Fine SL, Green WR. Clinicopathological correlation of drusen and retinal pigment epithelial abnormalities in age-related macular degeneration. *Retina.* 1994;14(2):130-142.

35.	Pichi F, Massaro D, Serafino M, et al. Retinal astrocytic hamartoma: optical coherence tomography classification and correlation with tuberous sclerosis complex. *Retina.* 2016;36(6):1199-1208.

36.	Sato T, Mrejen S, Spaide RF. Multimodal imaging of optic disc drusen. *Am J Ophthalmol.* 2013;156(2):275-282 e271.

37. Querques G, Georges A, Ben Moussa N, Sterkers M, Souied EH. Appearance of regressing drusen on optical coherence tomography in age-related macular degeneration. *Ophthalmology.* 2014;121(1):173-179.

38. Heiferman MJ, Fawzi AA. Discordance between blue-light autofluorescence and near-infrared autofluorescence in age-related macular degeneration. *Retina.* 2016;36 Suppl 1:S137-S146.

39. Oishi A, Thiele S, Nadal J, et al. Prevalence, natural course, and prognostic role of refractile drusen in age-related macular degeneration. *Invest Ophthalmol Vis Sci.* 2017;58(4):2198-2206.

40. Pang C, Messinger JD, Zanzottera EC, Freund KB, Curcio CA. The Onion Sign in neovascular age-related macular degeneration represents cholesterol crystals. *Ophthalmology.* 2015;122(11):2316-2326.

41. Verberckmoes SC, Persy V, Behets GJ, et al. Uremia-related vascular calcification: more than apatite deposition. *Kidney Int.* 2007;71(4):298-303.

42. Fischer DC, Behets GJ, Hakenberg OW, et al. Arterial microcalcification in atherosclerotic patients with and without chronic kidney disease: a comparative high-resolution scanning X-ray diffraction analysis. *Calcif Tissue Int.* 2012;90(6):465-472.

43. Lagier R, Baud CA. Magnesium whitlockite, a calcium phosphate crystal of special interest in pathology. *Pathol Res Pract.* 2003;199(5):329-335.

44. Kani T, Kani M, Moriwaki Y, Doi Y. Microbeam x-ray diffraction analysis of dental calculus. *J Dent Res.* 1983;62(2):92-95.

45. Tas AC. Synthesis of biomimetic Ca-hydroxyapatite powders at 37 degrees C in synthetic body fluids. *Biomaterials.* 2000;21(14):1429-1438.

46. Villa-Bellosta R. Impact of magnesium:calcium ratio on calcification of the aortic wall. *PLoS One.* 2017;12(6):e0178872.

47. Hogan MJ, Alvarado JA, Weddell JE. *Histology of the Human Eye. An Atlas and Textbook.* Philadelphia: W. B. Saunders; 1971.

48. Jensen OA. Bruch's membrane in pseudoxanthoma elasticum. Histochemical, ultrastructural, and x-ray microanalytical study of the membrane and angioid streak areas. *Albrecht Von Graefes Arch Klin Exp Ophthalmol.* 1977;203(3-4):311-320.

49. Gliem M, Fimmers R, Muller PL, et al. Choroidal changes associated with Bruch membrane pathology in pseudoxanthoma elasticum. *Am J Ophthalmol.* 2014.

50. Hirata I, Akamatsu M, Fujii E, Poolthong S, Okazaki M. Chemical analyses of hydroxyapatite formation on SAM surfaces modified with COOH, NH(2), CH(3), and OH functions. *Dent Mater J.* 2010;29(4):438-445.

51. Nancollas GH, LoRe M, Perez L, Richardson C, Zawacki SJ. Mineral phases of calcium phosphate. *Anat Rec.* 1989;224(2):234-241.

52. Linde A, Lussi A, Crenshaw MA. Mineral induction by immobilized polyanionic proteins. *Calcif Tissue Int.* 1989;44(4):286-295.

53. Raggio CL, Boyan BD, Boskey AL. In vivo hydroxyapatite formation induced by lipids. *J Bone Miner Res.* 1986;1(5):409-415.

54. Scotchford CA, Ali SY. Magnesium whitlockite deposition in articular cartilage: a study of 80 specimens from 70 patients. *Ann Rheum Dis.* 1995;54(5):339-344.

55. Scotchford CA, Ali SY. Association of magnesium whitlockite crystals with lipid components of the extracellular matrix in human articular cartilage. *Osteoarthritis Cartilage.* 1997;5(2):107-119.

56. Jahnen-Dechent W, Heiss A, Schafer C, Ketteler M. Fetuin-A regulation of calcified matrix metabolism. *Circ Res.* 2011;108(12):1494-1509.

57. Lau WL, Festing MH, Giachelli CM. Phosphate and vascular calcification: Emerging role of the sodium-dependent phosphate co-transporter PiT-1. *Thromb Haemost.* 2010;104(3):464-470.

58. Lederer E. Regulation of serum phosphate. *J Physiol.* 2014;592(18):3985-3995.

59.   Lehninger AL. Mitochondria and calcium ion transport. *Biochem J.* 1970;119(2):129-138.

60.   Boonrungsiman S, Gentleman E, Carzaniga R, et al. The role of intracellular calcium phosphate in osteoblast-mediated bone apatite formation. *Proc Natl Acad Sci U S A.* 2012;109(35):14170-14175.

61.   Feher J, Kovacs I, Artico M, Cavallotti C, Papale A, Balacco Gabrieli C. Mitochondrial alterations of retinal pigment epithelium in age-related macular degeneration. *Neurobiology of Aging.* 2006;27(7):983-993.

62.   Terluk MR, Kapphahn RJ, Soukup LM, et al. Investigating mitochondria as a target for treating age-related macular degeneration. *J Neurosci.* 2015;35(18):7304-7311.

63.   Nordgaard CL, Karunadharma PP, Feng X, Olsen TW, Ferrington DA. Mitochondrial proteomics of the retinal pigment epithelium at progressive stages of age-related macular degeneration. *Invest Ophthalmol Vis Sci.* 2008;49(7):2848-2855.

64.   Galluzzi L, Blomgren K, Kroemer G. Mitochondrial membrane permeabilization in neuronal injury. *Nat Rev Neurosci.* 2009;10(7):481-494.

65.   Kaneko H, Dridi S, Tarallo V, et al. DICER1 deficit induces Alu RNA toxicity in age-related macular degeneration. *Nature.* 2011;471(7338):325-330.

66.   Kerur N, Fukuda S, Banerjee D, et al. cGAS drives noncanonical-inflammasome activation in age-related macular degeneration. *Nat Med.* 2018;24(1):50-61.

67.   Miyagishima KJ, Wan Q, Corneo B, et al. In pursuit of authenticity: induced pluripotent stem cell-derived retinal pigment epithelium for clinical applications. *Stem Cells Transl Med.* 2016;5(11):1562-1574.

68.   Gomez NM, Lu W, Lim JC, et al. Robust lysosomal calcium signaling through channel TRPML1 is impaired by lysosomal lipid accumulation. *FASEB J.* 2017.

69.   Pattnaik BR, Hughes BA. Regulation of Kir channels in bovine retinal pigment epithelial cells by phosphatidylinositol 4,5-bisphosphate. *Am J Physiol Cell Physiol.* 2009;297(4):C1001-1011.

70.   Zhang X, Hughes BA. KCNQ and KCNE potassium channel subunit expression in bovine retinal pigment epithelium. *Exp Eye Res.* 2013;116:424-432.

71.   Gong H, Amemiya T, Takaya K. Retinal changes in magnesium-deficient rats. *Exp Eye Res.* 2001;72(1):23-32.

72.   Spraul CW, Lang GE, Grossniklaus HE, Lang GK. Histologic and morphometric analysis of the choroid, Bruch's membrane, and retinal pigment epithelium in postmortem eyes with age-related macular degeneration and histologic examination of surgically excised choroidal neovascular membranes. *Survey of Ophthalmology.* 1999;44 Suppl 1:S10-32.

73.   Hutcheson JD, Goettsch C, Bertazzo S, et al. Genesis and growth of extracellular-vesicle-derived microcalcification in atherosclerotic plaques. *Nat Mater.* 2016;15(3):335-343.

74.   Nakahara T, Dweck MR, Narula N, Pisapia D, Narula J, Strauss HW. Coronary artery calcification: from mechanism to molecular imaging. *JACC Cardiovasc Imaging.* 2017;10(5):582-593.

75.   Li CM, Presley JB, Zhang X, et al. Retina expresses microsomal triglyceride transfer protein: implications for age-related maculopathy. *Journal of Lipid Research.* 2005;46(4):628-640.

76.   Zheng W, Reem R, Omarova S, et al. Spatial distribution of the pathways of cholesterol homeostasis in human retina. *PLoS ONE.* 2012;7(5):e37926.

77.   Kakigi CL, Singh K, Wang SY, Enanoria WT, Lin SC. Self-reported calcium supplementation and age-related macular degeneration. *JAMA Ophthalmol.* 2015;133(7):746-754.

78.   Gopinath B, Flood VM, Louie JC, et al. Consumption of dairy products and the 15-year incidence of age-related macular degeneration. *Br J Nutr.* 2014;111(9):1673-1679.

79.   Klein R, Klein BE, Jensen SC, et al. Medication use and the 5-year incidence of early age-related maculopathy: the Beaver Dam Eye Study. *Arch Ophthalmol.* 2001;119(9):1354-1359.

80. Ferris FL, 3rd, Wilkinson CP, Bird A, et al. Clinical classification of age-related macular degeneration. *Ophthalmology.* 2013;120(4):844-851.

81. Schindelin J, Arganda-Carreras I, Frise E, et al. Fiji: an open-source platform for biological-image analysis. *Nat Methods.* 2012;9(7):676-682.

82. Li M, Dolz-Marco R, Messinger JD, et al. Clinicopathologic correlation of anti-vascular endothelial growth factor-treated type 3 neovascularization in age-related macular degeneration. *Ophthalmology.* 2018;125(2):276-287.

83. Mosselmans JF, Quinn PD, Dent AJ, et al. I18--the microfocus spectroscopy beamline at the Diamond Light Source. *J Synchrotron Radiat.* 2009;16(Pt 6):818-824.

84. Solé VA, Papillon E, Cotte M, Walter P, Susini J. A multiplatform code for the analysis of energy-dispersive X-ray fluorescence spectra. *Spectrochimica Acta Part B: Atomic Spectroscopy.* 2007;62(1):63-68.

85. Zanzottera EC, Messinger JD, Ach T, Smith RT, Freund KB, Curcio CA. The Project MACULA retinal pigment epithelium grading system for histology and optical coherence tomography in age-related macular degeneration. *Invest Ophthalmol Vis Sci.* 2015;56(5):3253-3268.

86. Zanzottera EC, Messinger JD, Ach T, Smith RT, Curcio CA. Subducted and Melanotic cells in advanced age-related macular degeneration are derived from retinal pigment epithelium. *Invest Ophthalmol Vis Sci.* 2015;56(5):3269-3278.

87. Dolz-Marco R, Glover JP, Litts KM, et al. Choroidal and sub-retinal pigment epithelium caverns: multimodal imaging and correspondence with Friedman lipid globules. *Ophthalmology.* 2018;4/8/18 online.

Figure 1: **Multi-modal imaging of 3 types of calcified structures in advanced AMD.** Heterogeneous internal reflectivity in drusen (HIRD), reflective dots, and plaques, seen on optical coherence tomography (OCT) (top), color fundus photography (CFP) (top middle), fundus autofluorescence (FAF) (bottom middle) and near-infrared imaging (NIR) (bottom). HIRD with a hyporeflective core (red arrow) and a hyperreflective cap (pink arrowhead), hyperreflective dots (green circle), and a hyperreflective plaque within Bruch's membrane (blue arrowhead) are indicated.
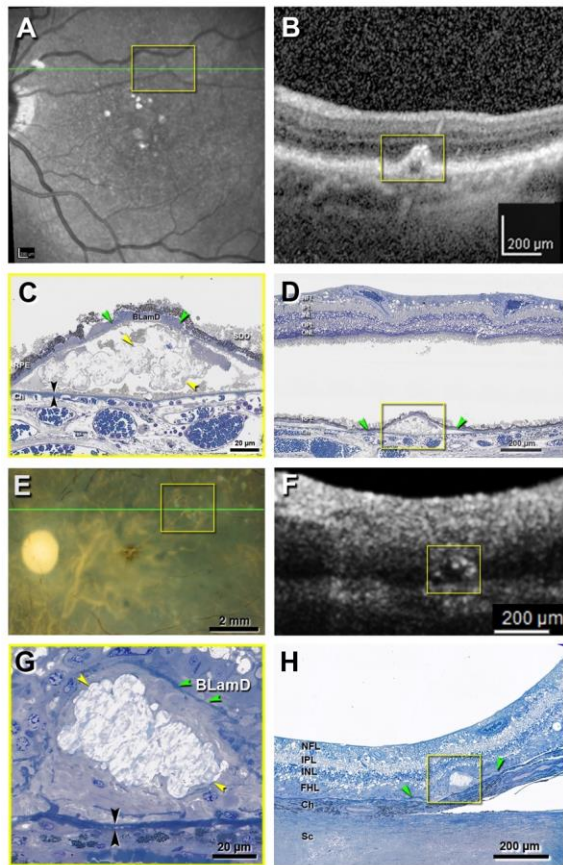
Figure 2: *In vivo* **and** *ex vivo* **imaging of heterogeneous internal reflectivity within drusen (HIRD) correlated to nodules in histology.** NFL, nerve fiber layer; IPL, inner plexiform layer; INL, inner nuclear layer; HFL, Henle fiber layer; ONL, outer nuclear layer; BLamD, basal laminar deposit (a thickening of basement membrane material between the RPE and its basement lamina); Ch, choroid; Sc, sclera. Yellow arrowheads, calcific nodules; green arrowheads, BLamD; Black arrowheads, Bruch's membrane. **A-D:** Eye of an 86-year-old white female with geographic atrophy (GA) imaged *in vivo* 4 months before death. **A.** NIR image shows translucent large drusen. Green line, level of optical coherence tomography (OCT) scan in panel B. Yellow frame, druse on panel **B-D**. **B.** OCT shows HIRD. **C.** Druse corresponding to the HIRD. Large refractile nodules are surrounded by lipid-rich soft druse material (gray). SDD, subretinal drusenoid deposits. **D.** Panoramic light microscopy. The HIRD of panel B and the druse are the same distance from the optic nerve head. **E-H.** Eye of a 94-year-old white female with GA, imaged *ex vivo*. **E.** Color fundus photography shows refractile drusen in the superior temporal quadrant. Green line, level of OCT scan in panel F. **F.** Yellow frame denotes an HIRD. **G.** Calcific nodules are surrounded by processes of Müller cells. Overlying BLamD is thin and fragmented. **H.** Context of calcified druse, showing degeneration of outer retina including gliotic Henle fiber layer and absent photoreceptors. Submicrometer epoxy resin sections of OTAP-post-fixed specimens, toluidine blue stain. Separation of retina from RPE (B) and choroid from sclera (H) is artifactual.
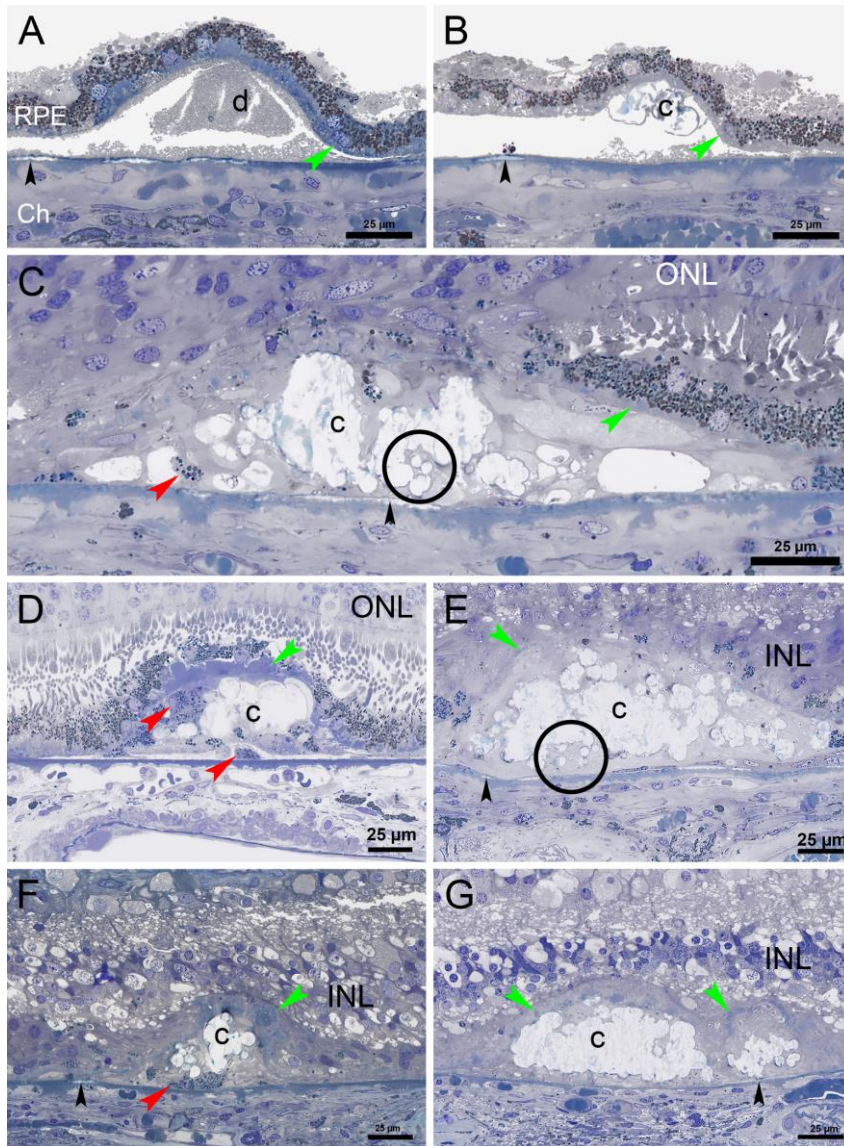
Figure 3**: Histological variants of calcific nodule formation and RPE degeneration in geographic atrophy.** Submicrometer epoxy resin sections of OTAP-post-fixed specimens, toluidine blue stain. INL, inner nuclear layer; ONL, outer nuclear layer; RPE, retinal pigment epithelium; green arrowheads, basal laminar deposit (BLamD); c, calcific nodule; black circle, calcific spherules; black arrowheads, calcification within Bruch's membrane; red arrowheads, RPE/ RPE derived material as indicated; Ch, choroid. **A.** Small soft druse (d) containing lipoprotein-derived debris (artifactually fractured) and intact overlying RPE. **B.** Small soft druse with partial contents, refractile nodules, and intact overlying RPE. **C.** Calcific nodules and spherules and RPE-derived granule aggregates, with partial covering of RPE and photoreceptors, and lacking BLamD. **D.** Druse with calcific nodules and nucleated 'subducted' RPE with thick overlying BLamD and nearly complete coverage by RPE. **E.** Calcific nodules with very thin BLamD and no RPE. **F.** Calcific nodules with thin BLamD and 'subducted' RPE. **G.** Calcific nodules with thin (left) and thick (BLamD)
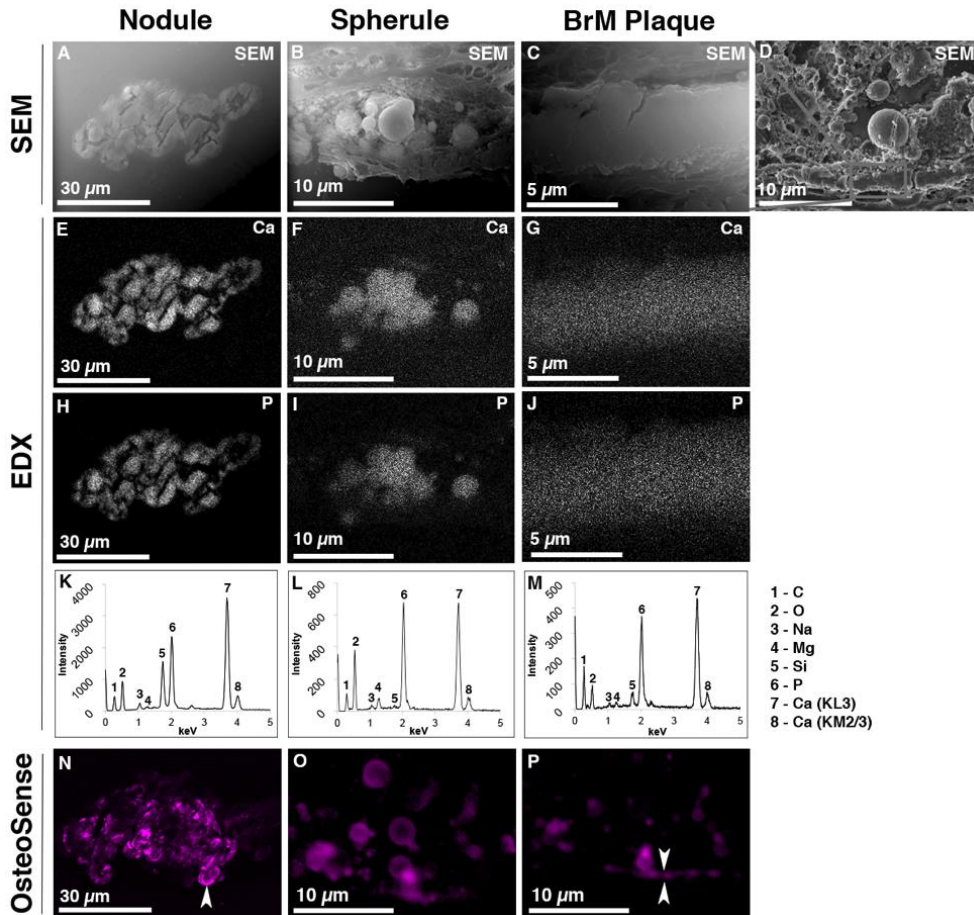
Figure 4: **Scanning electron microscopy and energy dispersive x-ray spectroscopy of nodules, spherules and plaques. A-D** High-magnification electron micrographs of calcific lesions. **A.** A nodule composed of lobed units ~1-5 µm in diameter. Cracks present on the nodule surface were formed during sectioning. **B.** Spherules approximately 0.5-5.0 µm in diameter were located between the basal lamina of the RPE and the inner collagenous layer of BrM. Extracellular material was also visible within deposits. **C.** Plaques, tens of microns in length, appeared visually similar to non-mineralized BrM. Cracks visible in the BrM indicated potential mineralization. **E-J.** Elemental maps of nodules, spherules and plaques generated using energy dispersive x-ray spectroscopy (EDX). **E-G.** Ca signaling was significantly greater in nodules, spherules and plaques compared to the background tissues. **H-J.** X-ray emissions specific to P were considerably greater in mineralized lesions compared to background. **K-M**. On EDX spectra, the most prominent peaks for nodules, spherules and plaques were 2.01 and 3.69 keV, these correlated to P (Peak 6) and Ca (Peaks 7, 8), respectively. In spherules and plaques, a small distinct peak characteristic of magnesium was also present (Peak 4), however this was greatly reduced in nodules. Peaks representative of organic tissues including carbon (Peak 1), oxygen (Peak 2), and sodium (Peak 3) were also present. Signals for C and O also originate from the calcific lesions. Silicon (Peak 5), a component of glass, was also detected. **N-P.** Hydroxyapatite-specific staining confirmed the presence of apatite in nodules, spherules and plaques (arrowheads delimit the BrM).
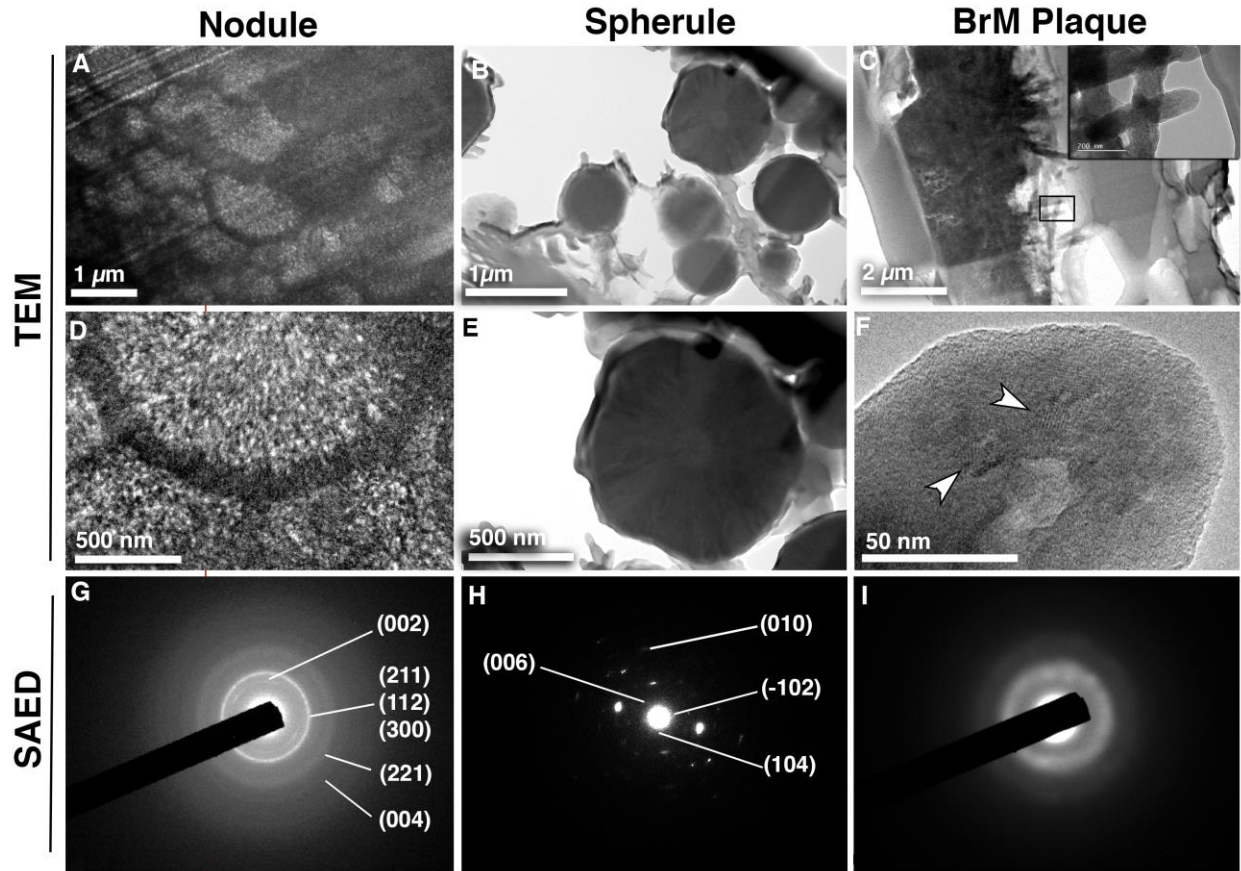
Figure 5: **Figure 5. Transmission electron microscopy and selected area electron diffraction of nodules, spherules and plaques. A-C.** Low magnification electron micrographs of nodules, spherules and plaques. **A.** Nodules were composed of multiple sub-units (lobes) 1-20 μm in diameter. **B.** Spherules 0.5-5 μm in diameter exhibited increased electron density. **C.** Plaques exhibited increased electron density and appeared crossed over and fibrous (inset image). **D-F.** High-magnification electron micrographs of calcific lesions associated with AMD. **D.** A single "lobe" sub-unit of a nodule. Each lobe has an electron dense crust and a less electron dense core. **E.** Spherules displayed a heterogeneous structure; needle crystal-like structures formed a shell surrounding a less electron dense core. **F.** High-resolution micrograph of a plaque. White arrowheads indicate regions where the lattice is visible. **G-I.** Selected area electron diffraction of nodules, spherules, and plaques. A typical diffraction pattern obtained from each lesion is shown. Supplementary Table 2 details additional reflexions identified by SAED but not indicated on figures. **G.** Nodules were indexed to HAP. A sharp diffraction ring for (002) was present, whilst a single diffuse ring was present for reflexions (211), (112) and (300). Rings characteristic of (221) and (004) were also observed. Diffraction patterns for the crust and the core were similar. **H.** The mineral component of spherules was identified as Whitlockite. Zone Axes (010) of Whitlockite was identified with vector points for (-102), (006) and (104). **I.** Diffraction patterns obtained for BrM plaques produced a diffuse ring characteristic of apatite.

CFP= color fundus photograph, FAF= fundus autofluorescence, NIR= near-infrared reflectance, OCT=optical coherence tomography
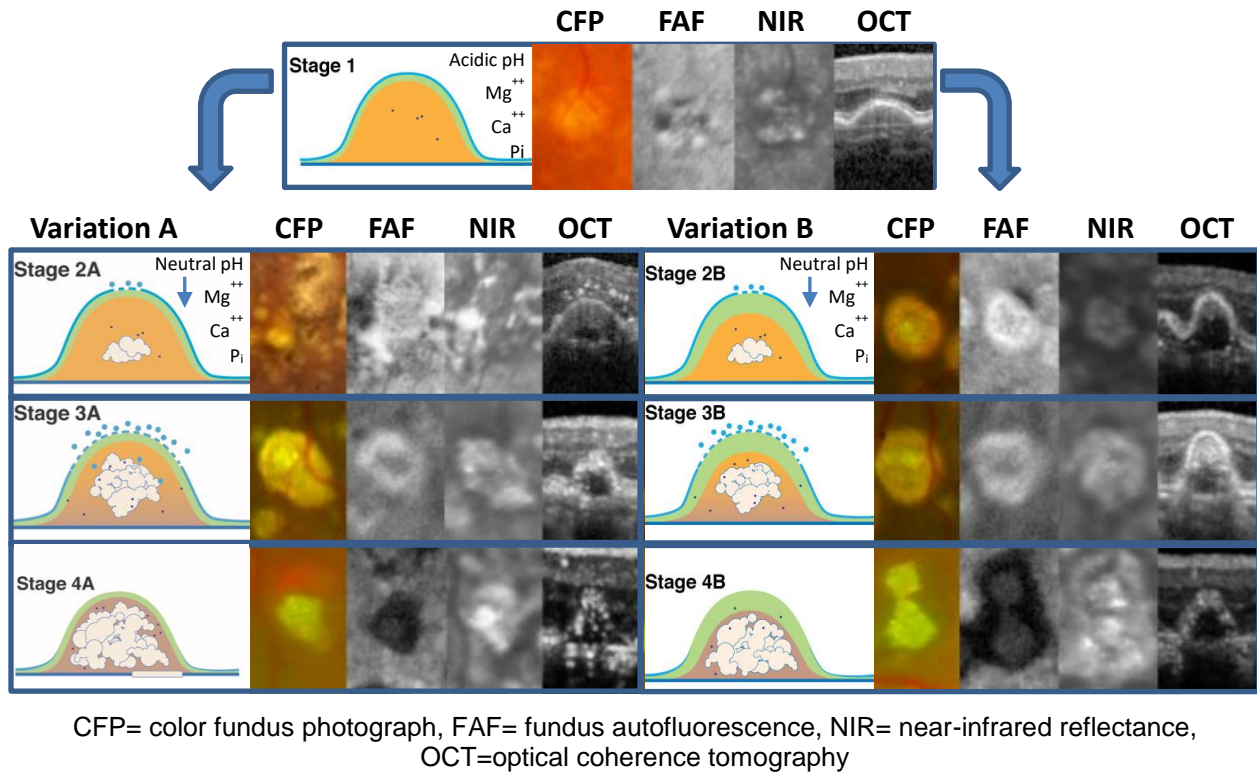
Figure 6: **Figure 6: Proposed progression stages of calcified structures in AMD.** Schematic (far left) and multimodal clinical imaging of nodule (white), HAP spherule (black) and BrM plaque (white) formation. **Stage 1:** Soft druse, no calcification, RPE intact (blue), with BLamD (green). Appears as non-glistening on CFP, isoautofluorescent on FAF, iso-reflective on NIR, and a hyperreflective intact RPE band overlying homogeneous sub-RPE contents on OCT. Extracellular environment has acidic pH; Mg^{+2}, Ca^{+2}, and inorganic phosphate is present. **Stage 2A:** Initiation of nodule formation. BLamD is present (above) and RPE migration occurs (blue dots). Appears as mostly non-glistening on CFP, mostly hyperautofluorescent on FAF, increasing focal areas of hyper-reflectivity on NIR and a hyporeflective area (nodule) within a druse with intact RPE on OCT. Extracellular environment has changed to neutral pH with lower levels of Mg^{+2}. **Stage 3A:** Focal areas of RPE atrophy (blue dotted line), more HAP spherules observed. Increasing glistening areas on CFP, hypoautofluorescent centers with surrounding hyperautofluorescent borders on FAF, hyperreflective on NIR, and a focal loss of hyperreflective RPE with surrounding hyperreflective dots (HAP spherules) on OCT. **Stage 4A:** Complete RPE loss, almost complete loss of druse contents, nodule with overlying thin veil of BLamD. Appears as a greater glistening area on CFP, a confluent area of hypoautofluorescence on FAF, hyperreflective on NIR, and complete loss of the RPE band with a hyporeflective core and a hyperreflective border on OCT. **Stage 2B, 3B and 4B:** Similar to respective "A" stage with a thicker BLamD cap (green) that appeared hyperreflective on OCT.

SUPPLEMENTARY MATERIAL:

Clinical and nano-analytical imaging identify calcified nodules as progression markers for age-related macular degeneration

Anna C.S. Tan, [#1,2,3,4] Matthew G. Pilgrim, [#5] Sarah Fearn,[6] Sergio Bertazzo,[7] Elena Tsolaki,[7]

Alexander P. Morrell,[8] Miaoling Li,[9] Jeffrey D. Messinger,[9] Rosa Dolz-Marco,[1,2]

Jianqin Lei,[10] Muneeswar G. Nittala,[10] Srinivas R. Sadda, [10, 11]

Imre Lengyel, [†*5,12] K. Bailey Freund, [*1,2,13] and Christine A. Curcio [*9]
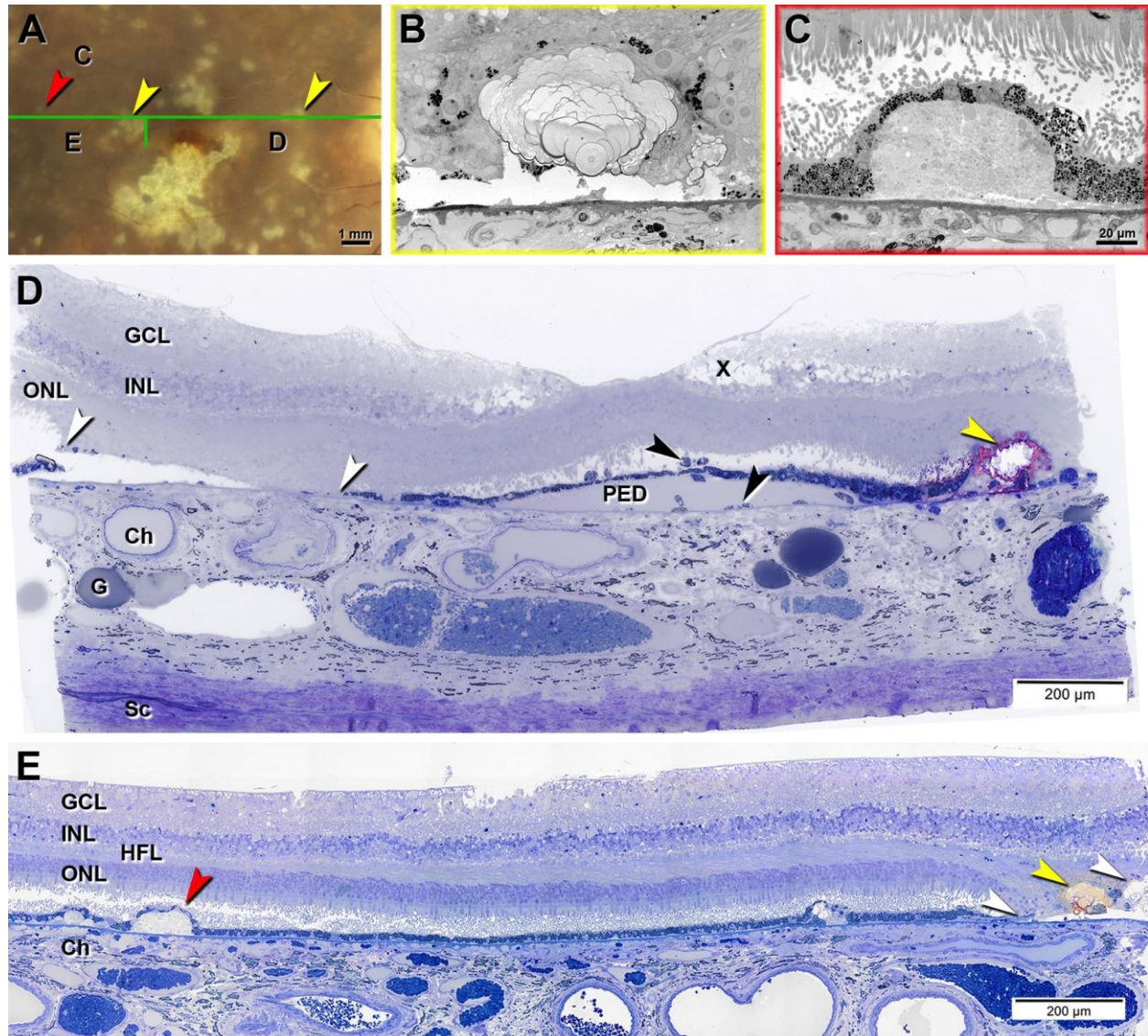
Figure S1: Refractile drusen with nodules and RPE atrophy in the index case for microanalysis. This 83-year-old white female donor had 20/60 vision recorded at last examination 7 months before death.[26] Submicrometer epoxy sections section of osmium-post-fixed specimen, toluidine blue stain. GCL, ganglion cell layer; INL, inner nuclear layer; HFL, Henle fiber layer, ONL, outer nuclear layer, Ch, choroid; Sc, sclera. **A.** *Ex vivo* color fundus photograph shows refractile drusen shown in panel D and E (yellow arrowheads), a soft druse (red arrowhead) and central RPE atrophy. Green line indicates section plane of panels D and E. **B.** Cumuloid druse with nodules, temporal to fovea, shown in panel E. **C.** Typical extrafoveal druse in this case. A similar druse is present in panel E. **D.** Panoramic view of section through superior edge of the foveal floor (segment D in panel A). PED, serous pigment epithelium detachment with overlying intact RPE and 'sloughed' and 'subducted' [85,86] RPE (top and bottom black arrowheads, respectively). X, post-mortem artifact. G, Friedman lipid globule [87]. Yellow arrowhead, refractile druse with nodules, some of which are dislodged. White arrowheads delimit atrophic area. **E.** Panoramic view of temporal perifovea (segment E in panel A). White arrowheads delimit atrophic area. Red arrowhead, soft druse. Yellow arrowhead, large refractile druse, also shown in Supplementary Figures 3 and 4.
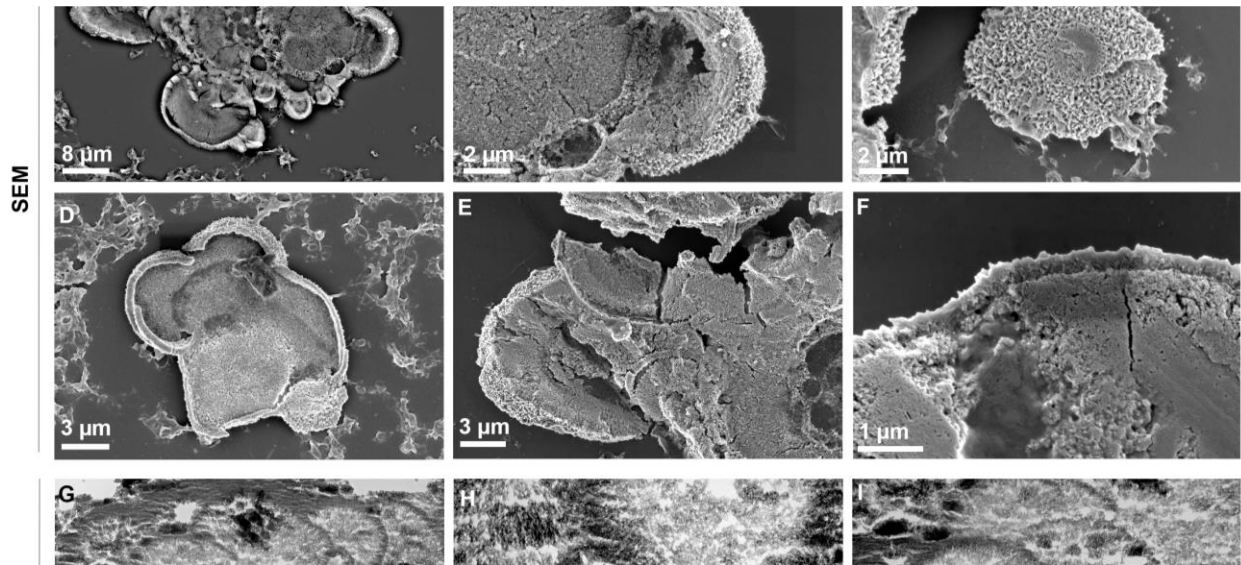
Figure S2. Scanning electron microscopy of isolated nodules. A-E. Isolated nodules embedded in epoxy resin were sectioned at 2 μm followed by etching with sodium methoxide. Electron micrographs were obtained using a secondary electron detector. **A.** Scanning electron micrograph of an isolated nodule. The lobed sub-units of nodules show great variation in size. Most have a distinct crust and core. **B and C.** Etching of the epoxy resin revealed the topographic structure of the nodule surface. Nodules had uneven surfaces reminiscent of a sponge-like tissue. **D.** A small isolated nodule also formed of smaller lobed subunits. Distinct crusts are also visible. **E and F.** High-magnification images showing the distinct crusts (arrowheads) present on each of the lobed sub-units.
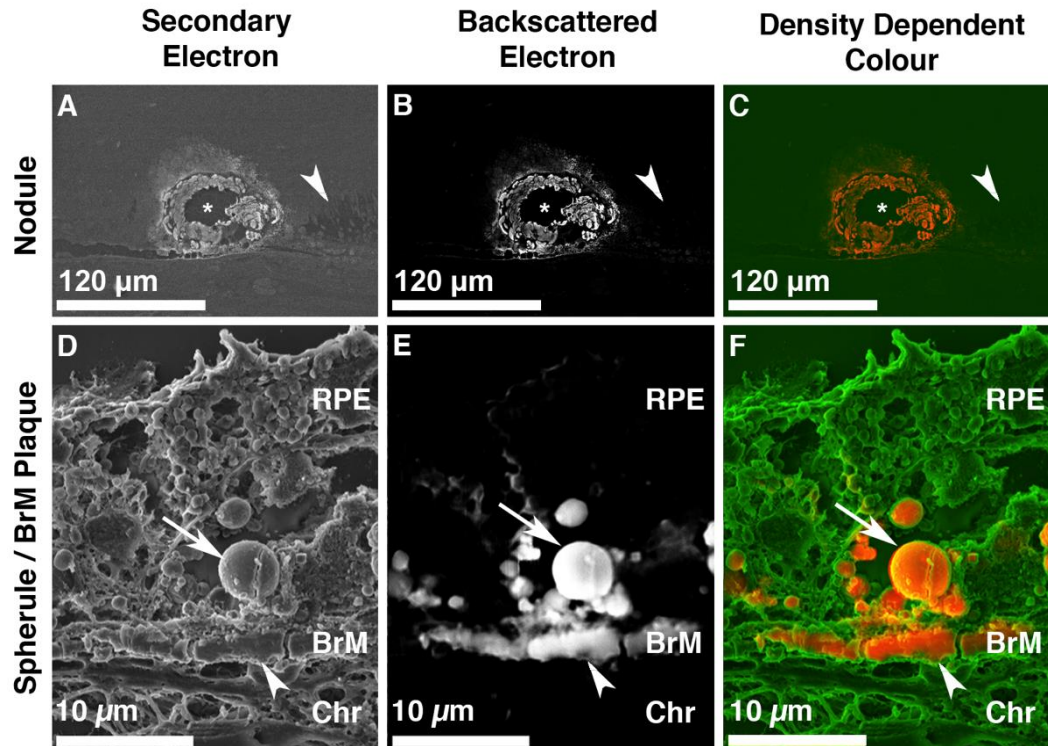
Figure S3. Density dependent color – scanning electron microscopy of calcific lesions.
A-F. Density dependent color-scanning electron microscopy (DDC-SEM) enables visualization of dense material (red/orange), likely mineral deposits, within soft tissues (green) **A.** A high-resolution secondary electron micrograph of a multi-lobed nodule that is ~80-100 μm in diameter. **B.** A backscattered image of the region imaged in A. The nodule and short regions of BrM appear white indicating dense material. The surrounding soft tissues are not visible suggesting they are composed of less dense biological material. **C.** The dense nodule appears red/orange whilst the surrounding soft tissues appear green. **A-C.** Arrowheads indicate atrophy of the photoreceptor layer and the outer most layers of the neural retina whilst the asterisk indicates a nodule region artifactually removed during processing. **D.** A secondary electron micrograph of a sub-RPE deposit containing a spherule (arrow) and a BrM plaque (Arrowhead). Note that the appearance of the plaque is similar to non-mineralized BrM when imaged with a secondary electron detector. **E.** A backscattered electron micrograph of the identical region imaged for D. Spherules and plaques appear white indicating dense material. The plaque displays intermittent mineralization along BrM. **F.** Spherules and BrM plaques appear red/orange indicating dense material. Extracellular materials within the sub-RPE deposit as well as the surrounding soft tissue appear green. RPE, retinal pigment epithelium; BrM, Bruch's membrane; Chr, Choroid.
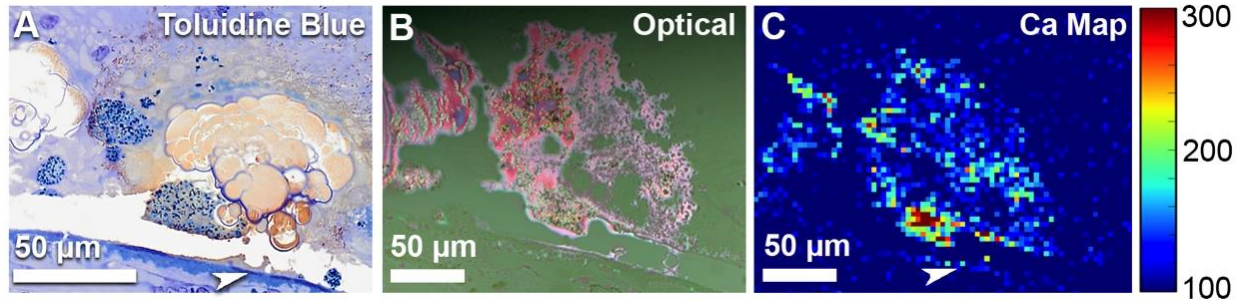
Figure S4. Synchrotron microfocus x-ray fluorescence confirms the presence of Ca in large nodules. A. A toluidine blue stained cross section containing a nodule. Increased toluidine blue staining in the BrM was observed (arrowhead), potentially indicating mineralization. An adjacent cross section of the same nodule was analysed by µXRF analysis. *Ex vivo* clinical images of this lesion are shown in Supplementary Figure 1. **B.** An optical image of the adjacent section. The purple and green coloration is due to the silicon nitride substrate. **C.** µXRF showing localization of Ca within nodules. Ca was also detected in the BrM (arrow head), correlated to the increased toluidine blue staining observed in A.
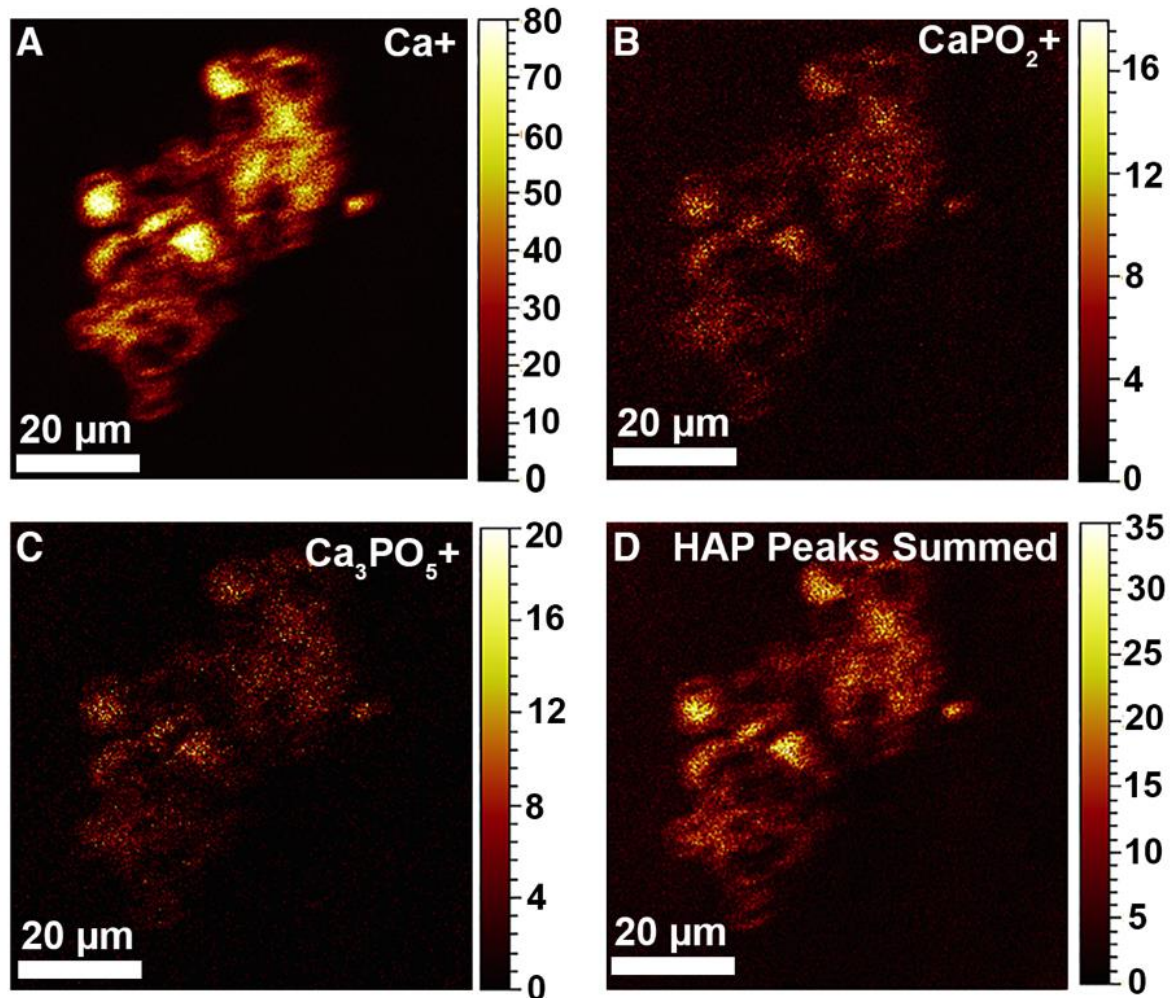
Figure S5. Time of flight-secondary ion mass spectrometry confirms the presence of calcium phosphate within nodules. A-C. Secondary molecular ion maps of Ca+, $CaPO_2$+, Ca_3PO_5+ confirmed the localization of calcium and phosphate within nodules. **D.** A secondary molecular ion map of summed calcium phosphate peaks indicative of hydroxyapatite. Secondary ions include: 39.9 m/z, $[Ca^+]$; 55.9 m/z, $[CaO^+]$; 102.9 m/z, $[CaPO_2^+]$; 158.9 m/z, $[Ca_2PO_3^+]$; 174.9 m/z, $[Ca_2PO_4^+]$; and 230.8 m/z, $[Ca_3PO_5^+]$. Scale bars: A-D 20 μm.
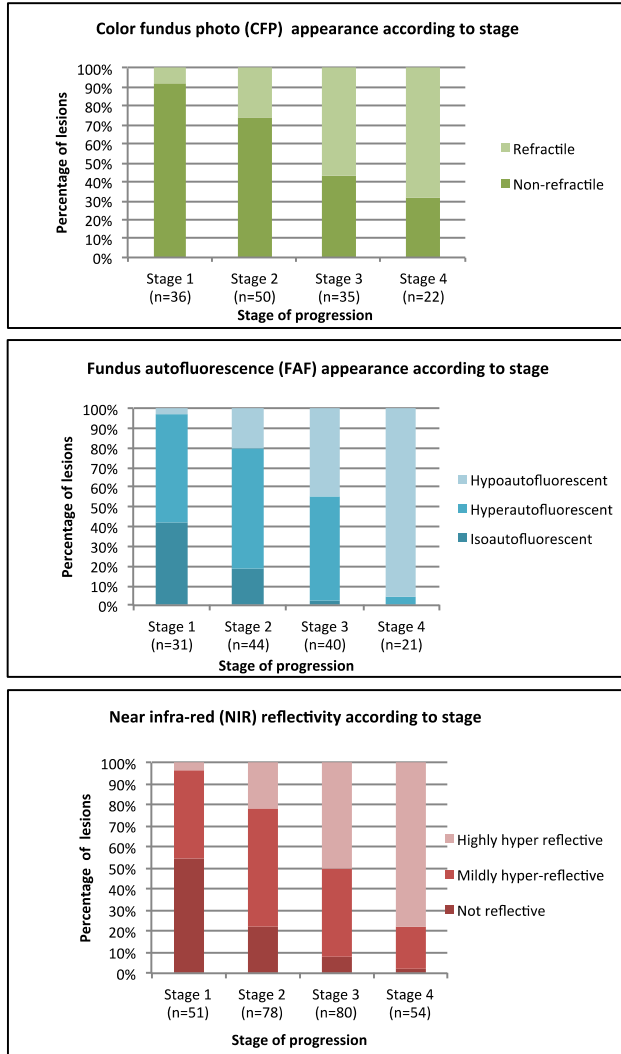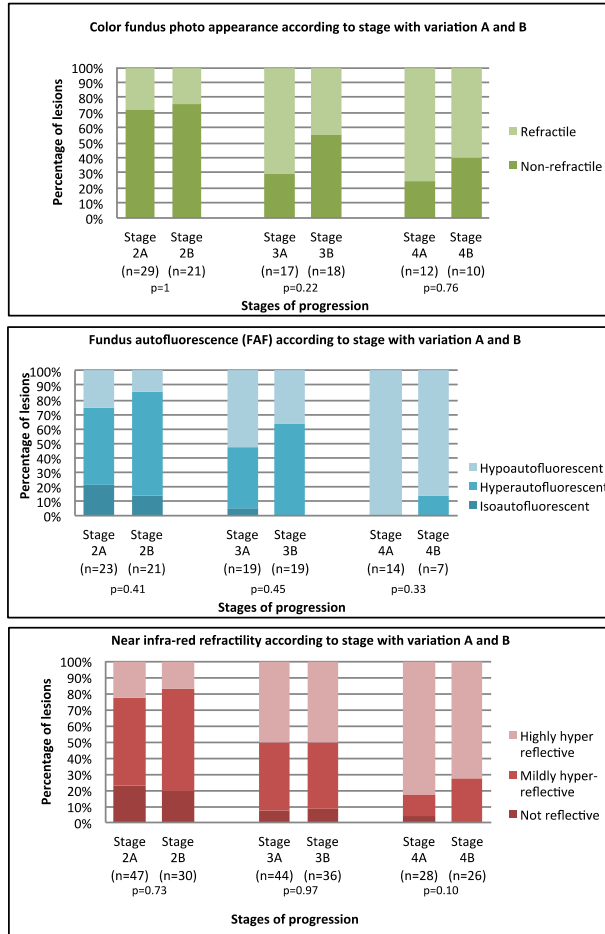
Figure S6: Appearance of heterogeneous internal reflectivity in drusen (HIRD) as seen on multimodal imaging during progression. N = number of lesions seen at each stage where the relevant imaging is available. CFP (top) shows increased percentage of glistening dots over the HIRD as the overlying RPE is lost, thus exposing hyperreflective dots (HAP spherules) at the surface. FAF (middle) shows increased hypoautofluorescence as the overlying RPE is lost. NIR imaging shows an increasing percentage of highly refractile HIRD as the overlying RPE is lost and HAP spherules in drusen are exposed.

Figure S7: Appearance of heterogeneous internal reflectivity in drusen (HIRD) in variation A and B as seen on multi modal imaging during progression. N = number of lesions seen at each stage where the relevant imaging is available. No statistically significant difference (p>0.05) was seen (chi-square test) between the appearance at each stage. Subtle differences exist mostly in Stage 4 where the RPE is lost and a thin (Variation A) or thick (Variation B) basal lamina deposit is exposed. CFP (top) shows that at Stage 4B compared to Stage 4A, fewer HIRD are glistening, which may be due to HAP spherules covered by BLamD. FAF (middle) of Stage 4B shows more hyperautofluorescence than Stage 4A. NIR imaging shows a smaller percentage of highly hyper-reflective HIRD in Stage 4B versus 4A.

Table S1: Composition and appearance of calcified structures in eyes with geographic atrophy as revealed by multi-modal clinical and molecular imaging.

	Spherules	Nodules	Plaques
Composition	Hydroxyapatite	Calcium, phosphate, silicon	Calcium phosphate
Light microscopy, ≤2000X viewing magnification	Refractile, spheres	Refractile, lobular	Refractile, horizontal plaque in the 3 middle layers of Bruch's membrane, not in the basal laminas of RPE or choriocapillaries
	Clinical multi-modal imaging		
Color fundus photo	Glistening, reflective	Yellow, non-glistening	Glistening, reflective
Near-infrared reflectance	Hyperreflective	Iso/hyperreflective	Hyperreflective
Fundus autofluorescence	Not seen	Within areas of hypoautofluorescence	Within areas of hypoautofluorescence
Optical coherence tomography	Hyperreflective dots	Hyporeflective core	Hyperreflective line
	Molecular multi-modal imaging		
In lens scanning electron microscopy	0.5-5 µm diameter, isolated or clustered, heterogeneous surface structure	Multiple lobes, a single lobe is typically larger than a spherule, overall ≤100 µm diameter, heterogeneous surface structure	Indistinguishable from non-mineralized BrM
Backscatter scanning electron microscopy	0.5-5 µm diameter, spherules appear white, soft tissue appears black	A white crust highlights the edge of each lobe, fragments within the lobes have reduced brightness, soft tissue appears black	BrM appears white at sites of mineralization, soft tissue appears black
Transmission electron microscopy	0.5-5 µm diameter, solid spherical particles are electron dense compared to biological tissue, variation in electron density within spherules	Multi-lobed solid structure. Lobes vary in size from 1-20 µm, lobes have a highly electron dense crust and a less dense core. High magnification reveals small crystal like particles	BrM plaques are electron dense, have a feathery cross-hatched appearance related to collagen fibrils at low magnifications. At high magnifications, the lattice structure can be observed at isolated regions

Table S2: D spacings and I/Imax (%, 3 d.p.) of candidate calcium phosphate compounds.

A table detailing D-spacings (angstroms) and relative intensities of zone axes reflections (I/Imax) for several candidate calcium phosphates. D-spacings calculated from collected SAED of nodules, BrM plaques, and spherules are highlighted in orange cells. D-spacings were obtained from multiple diffraction patterns from the same lesion. D-spacings obtained for nodules and BrM plaques are more similar to HAP than to Fluorapatite, Monetite, OCP, B-TCP and Brushite.

Planes	Nodule d [A]	BrM Plaque d [A]	HAP d [A]	HAP I/Imax	Fluorapatite d [A]	Fluorapatite I/Imax	Monetite d [A]	Monetite I/Imax	Octacalcium Phosphate d [A]	Octacalcium Phosphate I/Imax	Beta-Tricalcium phosphate d [A]	Beta-Tricalcium phosphate I/Imax	Whitlockite d [A]	Whitlockite I/Imax	Brushite d [A]	Brushite I/Imax
2 0 0		4.0241	4.0794	2.588	4.0621	5.547	3.3579	62.421	9.3184	0.699					2.6023	91.767
0 2 0			4.0794	2.588	4.0621	5.547	3.2902	0.762	4.5108	0.106					7.5900	70.021
0 2 1			3.5090	0.782	3.4988	0.558	2.8399	17.014	3.7332	11.141						
2 0 1			3.5090	0.782	3.4988	0.558			5.3862	1.410						
0 0 2	3.4344	3.4503	3.4400	100.000	3.4435	82.554	3.3543	10.296	3.4136	96.226					2.7934	3.396
1 0 -2		3.1621	3.1698	6.371	3.1705	4.505	2.7512	5.078	3.3297	0.005						
2 1 0		3.0721	3.0837	10.612	3.0707	1.152	2.9951	51.827	5.6414	0.200	5.2175	8.517	5.1650	0.003		
2 1 1	2.8110		2.8140	38.371	2.8045	14.888	2.5042	0.156	4.2660	6.682	3.4015	1.135	3.3673	1.135	2.0192	8.015
3 0 0	2.7211		2.7196	79.948	2.7081	59.781	2.2386	0.266	6.2123	0.153	3.0123	12.333	2.9820	2.477		
0 3 0	2.7211		2.7196	79.948	2.7081	59.781	2.1935	0.668	3.0072	17.037	3.0123	12.333	2.9820	2.477		
3 1 0			2.2629	4.770	2.2532	25.992	2.1215	0.653	4.4889	0.162						
1 0 4		1.6882	1.6830	1.952	1.6843	0.709	1.5434	0.234	1.6924	0.116	6.4982	4.874	6.4392	23.506		
0 0 6	6.1497		1.1467	25.368	1.1478	29.717	1.1181	0.016	1.1379	14.657	6.2338	2.886	6.1838	0.352		

MOVIE S1: Serial eye-tracked optical coherence tomography scans to document the progression of nodules, spherules and Bruch's membranes plaques over 6 years. Multiple similar videos were used to observe the progression of individual lesions over time.